remote sensing

MDPI

Article

Canopy Chlorophyll Retrieval in Structurally Complex Pedunculate Oak Forests: Empirical Machine Learning Versus Hybrid PROSAIL–GPR

Nikola Zorić [1,*], Anita Simic Milas [2], Jochem Verrelst [3], Dinka Matošević [1], Ante Seletković [4] and Ivan Balenović [5]

[1] Division for Forest Protection and Game Management, Croatian Forest Research Institute, Cvjetno Naselje 41, 10450 Jastrebarsko, Croatia
[2] School of Earth, Environment and Society, Bowling Green State University, 190 Overman Hall, Bowling Green, OH 43403, USA
[3] Image Processing Laboratory (IPL), University of Valencia, Catedrático Agustín Escardino Benlloch 9, 46980 Paterna, Spain
[4] Faculty of Forestry and Wood Technology, University of Zagreb, Svetošimunska Cesta 23, 10000 Zagreb, Croatia
[5] Division for Forest Management and Forestry Economics, Croatian Forest Research Institute, Cvjetno Naselje 41, 10450 Jastrebarsko, Croatia
* Correspondence: nikolaz@sumins.hr

Highlights

What are the main findings?

- Gaussian Process Regression (GPR) provided the most accurate retrieval of canopy chlorophyll content (CCC) from four-band UAV multispectral imagery in most of the evaluated oak stands and phenological stages.
- The hybrid PROSAIL–GPR approach did not improve CCC retrieval and showed substantially lower accuracy, particularly during July and September.

What are the implications of the main findings?

- Under structurally complex forest conditions and limited spectral information, a physically constrained approach may underperform when the radiative-transfer model does not adequately represent three-dimensional canopy structure.
- Empirical GPR provided spatially explicit CCC estimates that resolved within-stand canopy heterogeneity and may support targeted assessment of forest physiological condition.

Abstract

Hybrid radiative transfer model–machine learning (RTM–ML) approaches can incorporate physical constraints into vegetation-trait retrieval, but their advantage over empirical learning remains uncertain for very-high-resolution, limited-band observations of structurally heterogeneous forest canopies. We compared six empirical machine-learning regression algorithms with a hybrid PROSAIL–Gaussian Process Regression (GPR) approach for retrieving derived canopy chlorophyll content (CCC) from four-band UAV multispectral imagery of pedunculate oak (*Quercus robur* L.) stands under contrasting oak lace bug (*Corythucha arcuata*) pressure. CCC was derived from field-derived leaf chlorophyll content and UAV-estimated leaf area index. Data were collected across three sampling periods from 2021 to 2023, and models were evaluated using tree-grouped three-fold cross-validation to maintain independence between training and held-out trees. Empirical performance varied among algorithms, sites, and sampling periods. At the infested site, GPR provided

Check for updates

Academic Editors: Eben N. Broadbent, Huaqiang Du and Dongdong Wang

Received: 19 August 2026
Revised: 12 October 2026
Accepted: 27 October 2026
Published: 29 October 2026

Copyright: © 2026 by the authors. Licensee MDPI, Basel, Switzerland. This article is an open access article distributed under the terms and conditions of the Creative Commons Attribution (CC BY) license.

the strongest performance in May (R^2 = 0.61, RMSE = 27.04 μg cm^{-2}, NRMSE = 10.87%), whereas Random Forest performed best in September. At the reference site, Random Forest, least-squares linear regression, and kernel ridge regression provided the strongest results depending on sampling period and performance metric, with R^2 reaching 0.60. According to the primary cross-validated predictive metrics (R^2, RMSE, and NRMSE), the tested PROSAIL–GPR approach generally showed lower predictive performance than the empirical models under the same tree-grouped evaluation framework. Empirical GPR maps resolved substantial within-stand spatial variation in derived CCC. Overall, incorporating PROSAIL-simulated information did not improve predictive performance under the tested four-band, crown-scale configuration. Rather than identifying a single cause, the results indicate that the benefit of physically constrained retrieval depends on compatibility among model representation and parameterization, canopy structure, spectral information, and available training data.

Keywords: canopy chlorophyll content; UAV multispectral imagery; empirical machine learning; hybrid RTM–ML retrieval; PROSAIL; Gaussian Process Regression; pedunculate oak; oak lace bug

1. Introduction

Forest ecosystems across Europe are increasingly affected by invasive insect pests, whose outbreaks can alter foliar condition before defoliation or crown dieback becomes visible. Early detection is therefore important because management options become more limited once damage is structurally expressed [1,2]. Remote sensing can contribute to early assessment by detecting physiological responses to stress, including changes in canopy pigments, rather than relying solely on visible structural symptoms. Unmanned aerial vehicles (UAVs) are particularly suited to this purpose because their very high spatial resolution enables canopy variability to be characterized at crown and within-stand scales in structurally heterogeneous forests [3,4].

Two complementary approaches are commonly used to retrieve vegetation traits from spectral observations. Empirical machine-learning regression algorithms (MLRAs) establish statistical relationships between measured reflectance and reference observations without explicitly representing the physical processes governing radiative transfer. They are computationally efficient and can achieve high predictive accuracy when the calibration data adequately represent the conditions to which the models are applied [5–8]. UAV-based machine-learning approaches have been applied to forest-health assessment, including quantification of pine processionary moth defoliation and detection of pine wilt disease [9,10], and data-driven methods are increasingly used in UAV-based forest-health workflows [3,4]. Their principal limitation is transferability, because performance may decline when canopy structure, illumination, phenology, or environmental conditions differ from those represented in the calibration data.

Radiative transfer models (RTMs) provide an alternative by explicitly representing relationships between vegetation properties and reflected radiation [11,12]. PROSAIL, which couples the PROSPECT leaf optical model with the SAIL canopy radiative-transfer model, is among the most widely used RTM frameworks for vegetation-trait retrieval [13]. Its standard formulation represents vegetation as a horizontally homogeneous turbid medium characterized by a prescribed leaf-angle distribution. This representation is less well matched to forests, where foliage is organized within branches and discrete crowns separated by gaps [14]. Crown clumping, mutual and within-crown shading, woody components, understory contributions, and multiple scattering can produce differences between simulated

and observed forest reflectance [15–19]. Forest-specific adaptations have therefore been developed to better represent these structural effects [20,21], and model intercomparison studies have demonstrated substantial variation among radiative-transfer formulations in simulated forest reflectance [22].

RTM-based approaches have nevertheless been successfully applied to structural and biochemical trait retrieval in heterogeneous forests, including oak and tropical forests [23–27], as well as to vegetation stress associated with insect and disease disturbance [28,29]. Hybrid approaches combine physical and empirical modeling by training machine-learning algorithms on RTM-simulated spectra, thereby incorporating physically based information while retaining the computational advantages of machine learning [30–33]. Such approaches have been successfully applied in agricultural and grassland canopies [32,34,35] and have more recently been extended to forest applications using UAV and airborne imagery [36–38].

Recent studies have further examined the influence of canopy structure and observational characteristics on PROSAIL-based retrieval. Zhou et al. [37] demonstrated the application of PROSAIL coupled with machine learning for forest canopy parameter estimation, while Zhang et al. [39] showed that removing canopy shadows improved LAI and chlorophyll retrieval from UAV multispectral imagery of individual apple-tree crowns. Xu et al. [40] reported improved leaf chlorophyll estimation by incorporating structural constraints into PROSAIL using airborne hyperspectral and LiDAR observations. These findings highlight the importance of canopy representation and structural information in physically based retrieval.

More recently, Zhao et al. [41] compared a three-dimensional radiative-transfer approach with conventional PROSAIL for fine-scale leaf chlorophyll retrieval, demonstrating the potential benefits of explicitly representing forest canopy structure. Zhang et al. [42] further developed a physics-guided transfer-learning framework integrating UAV multispectral and LiDAR observations with radiative-transfer simulations for three-dimensional forest chlorophyll retrieval. Their results demonstrated improved performance relative to several conventional retrieval approaches under the investigated conditions. Collectively, these studies establish the potential of physically informed retrieval while indicating that its effectiveness depends on canopy representation, spectral information, and the integration of simulated and observed data.

Despite these advances, the relative predictive advantage of hybrid over empirical retrieval remains insufficiently established for very-high-spatial-resolution, four-band UAV observations of structurally heterogeneous forest crowns. Previous studies have demonstrated the benefits of structural constraints, shadow correction, hyperspectral observations, and three-dimensional canopy modeling [37,39–42], but these findings do not necessarily establish that PROSAIL-based hybrid approaches outperform empirical models under more spectrally limited conditions. At crown scale, gaps, shadows, crown boundaries, and within-crown structural variability are explicitly resolved, while limited spectral dimensionality may restrict the ability to distinguish biochemical and structural properties producing similar reflectance. Consequently, the benefit of incorporating RTM-simulated information may depend on the compatibility between model assumptions, canopy structure, and available spectral information. A direct empirical–hybrid comparison using consistent observations, a common derived response variable, and tree-independent validation is therefore needed to assess their relative predictive performance and practical limitations.

Pedunculate oak (*Quercus robur* L.) stands affected by oak lace bug (OLB; *Corythucha arcuata*) provide an informative system in which to examine this question. OLB is established across European oak ecosystems [43–45], and its feeding can reduce photosynthetic performance and alter pigment composition in pedunculate oak [46,47]. Such physiological

changes, together with the structural heterogeneity of mature oak crowns, provide a relevant setting for evaluating CCC retrieval from very-high-resolution UAV observations. However, because OLB abundance and damage severity were not quantitatively measured in the present study, the contrasting stands are used to evaluate CCC retrieval under different canopy conditions rather than to establish a quantitative relationship between CCC and OLB infestation severity.

The specific contribution of this study is therefore not the development of a new machine-learning or radiative-transfer algorithm, but a controlled comparison of established empirical and hybrid approaches under a challenging and comparatively underexamined sensor–canopy configuration: four-band, very-high-spatial-resolution UAV observations of structurally heterogeneous mature oak crowns. Six empirical regression algorithms and a PROSAIL–GPR hybrid approach were evaluated using the same four-band UAV spectral space and derived CCC response variable, with models developed separately by site and sampling period and evaluated using tree-grouped cross-validation to maintain independence between training and held-out trees. For the hybrid approach, active learning and LUT optimization were performed independently within each training fold, with observations from held-out trees excluded from model development.

Accordingly, the study addresses three questions: (1) how does empirical CCC retrieval performance vary among regression algorithms, sites, and sampling periods under tree-grouped validation; (2) does the tested PROSAIL–GPR approach provide a predictive advantage over empirical retrieval when both are evaluated using the same four-band UAV observations and held-out trees; and (3) to what extent do the resulting CCC predictions characterize spatial variation in the derived canopy-level chlorophyll metric within the studied stands? Together, these questions evaluate whether incorporating physically based simulated information provides an advantage over direct empirical learning under the specific spectral, spatial, and canopy conditions examined here.

2. Data and Methods

2.1. Study Sites

The study was conducted at two pedunculate oak (*Quercus robur* L.) forest sites in Croatia selected to represent contrasting levels of oak lace bug (OLB; *Corythucha arcuata*) pressure within pedunculate oak-dominated stands. Site selection was based on information provided by Croatian Forests Ltd. (Zagreb, Croatia) and considered stand age, the proportion of oak in the species composition, and tree density (trees ha^{-1}).

Site A, hereafter referred to as the infested site, is located within the Karlovac Forest Administration (Jastrebarsko Forest Office; 45.6193°N, 15.6880°E; WGS84), where sustained OLB infestation and visible canopy damage were observed throughout the study period. Site B, hereafter referred to as the reference site, is located within the Buzet Forest Administration (Buzet Forest Office; 45.34134°N, 13.89392°E; WGS84). Although OLB has been reported in the Buzet region [48] and individual specimens were observed at Site B, OLB pressure remained low and no visible canopy damage was observed during the study period. Site B was therefore considered a reference stand with minimal OLB pressure rather than a strictly pest-free site (Figure 1).

Site A covers 107.38 ha and forms part of a long-term research site for monitoring carbon dioxide exchange. The site has a temperate, warm, and humid climate (Cfa), with mean summer temperatures exceeding 22 °C. Pedunculate oak is the dominant species, with a standing wood volume of 170.54 m^3 ha^{-1}, followed by narrow-leaved ash (*Fraxinus angustifolia*) and common hornbeam (*Carpinus betulus*). Site B covers 12.8 ha and has the same Cfa climate classification. The stand has a closed canopy and an average age of 65 years. Pedunculate oak is the dominant species, with a standing wood volume of 149.38 m^3 ha^{-1},

while narrow-leaved ash is the principal secondary species. Both sites are characterized primarily by alluvial and mineral-swampy soils and have a 140-year rotation period.

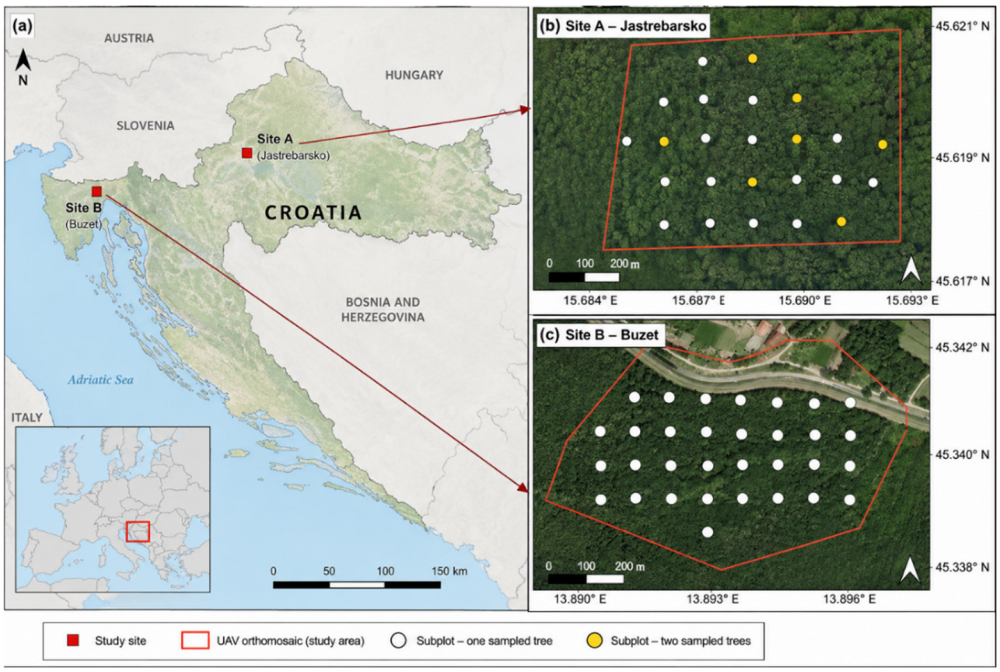


Figure 1. (**a**) Locations of the two study sites in Croatia. (**b**) Site A, Jastrebarsko (45.6193°N, 15.6880°E), the infested site, where sustained oak lace bug (OLB; *Corythucha arcuata*) infestation and visible canopy damage were observed throughout the study period. (**c**) Site B, Buzet (45.3413°N, 13.8939°E), the reference site, where OLB pressure remained low and no visible canopy damage was observed during the study period. Circles indicate sampling subplots.

The two sites differed not only in OLB pressure but also in geographic location and associated site conditions. Consequently, comparisons between Sites A and B are used to characterize differences in canopy condition and CCC retrieval performance and are not interpreted as evidence of a causal effect of OLB infestation.

2.2. Field and UAV Data

Field measurements were conducted over three consecutive years (2021–2023), with campaigns in May, July, and September to capture contrasting phenological stages and seasonal variation in canopy condition. Site A was monitored throughout the study period, whereas Site B was included as a reference site beginning in 2022. September 2023 observations at Site B were excluded from modeling because corresponding UAV reflectance data were unavailable. Field campaigns combined leaf-level chlorophyll content with UAV multispectral observations to spatially and temporally link leaf biochemical information, canopy structure, and remotely sensed reflectance.

Field measurements were conducted within an established system of 53 subplots, comprising 23 subplots at Site A and 30 at Site B. Two trees were sampled in selected subplots at Site A, as indicated in Figure 1. The coordinates of all sampled trees were recorded using GNSS-RTK positioning to enable accurate spatial correspondence between field measurements and UAV observations.

UAV imagery was acquired immediately before leaf sampling during each field campaign to minimize temporal differences between field and remotely sensed observations. A fixed-wing eBee SQ UAV (senseFly SA, Cheseaux-sur-Lausanne, Switzerland) equipped with a Parrot Sequoia multispectral camera (Parrot SA, Paris, France) and integrated RGB

sensor was used for image acquisition. The multispectral sensor recorded four bands centered in the green (550 nm), red (668 nm), red-edge (735 nm), and near-infrared (790 nm) regions. Three ground control points (GCPs) were distributed throughout each flight area and surveyed using a Stonex S900 GNSS-RTK receiver (Stonex Srl, Paderno Dugnano, Italy) connected to the CROPOS positioning service, with declared horizontal and vertical accuracies of 2 and 4 cm, respectively. Radiometric calibration was performed using a reference calibration panel recorded before and after each flight. Flights were planned in eMotion Ag (senseFly SA, Cheseaux-sur-Lausanne, Switzerland) at 100 m above ground level with 80% forward and 75% side overlap, resulting in a ground sampling distance of approximately 10 cm. These acquisition parameters were maintained across campaigns. No resampling to a common spatial resolution among campaigns was performed; the multispectral reflectance mosaics were analyzed at their native approximately 10-cm spatial resolution.

UAV acquisitions were conducted separately during the May, July, and September field campaigns, resulting in differences in solar illumination geometry among acquisition dates. Solar zenith angles ranged from 33° to 51° at Site A and from 34° to 55° at Site B. Over structurally heterogeneous forest canopies, these differences may influence measured reflectance through variation in illumination, crown shadowing, and bidirectional reflectance effects. No explicit bidirectional reflectance distribution function (BRDF) correction was applied. Models were therefore developed separately for each site and sampling month rather than pooling observations across phenological stages and acquisition geometries.

UAV imagery was processed in Pix4Dmapper (version 4.9.0; Pix4D SA, Prilly, Switzerland) using Structure-from-Motion (SfM) and Multi-View Stereo (MVS) photogrammetry to reconstruct scene geometry and generate georeferenced reflectance mosaics. The resulting products were analyzed in QGIS (version 3.40; QGIS Development Team), where spectral information was extracted from manually delineated crown-aspect polygons corresponding to the field sampling locations.

The canopy height model (CHM) was calculated by subtracting the digital terrain model (DTM) from the digital surface model (DSM), both generated from the UAV imagery using the Pix4D photogrammetric workflow. In closed-canopy forest conditions, reconstruction of the terrain surface from optical UAV imagery is limited by the availability of visible ground points within canopy gaps. Consequently, uncertainty in the photogrammetrically derived DTM propagates into the resulting CHM, particularly where ground observations are sparse or absent. The CHM was therefore not interpreted as an independently validated measure of absolute tree height. Instead, it was used as a relative representation of canopy height for identifying upper-canopy crown surfaces. A conservative 10 m CHM threshold was applied as a canopy-masking criterion to exclude low vegetation, understory, canopy gaps, and ground-related surfaces while retaining the upper-canopy portions of the sampled mature oak crowns.

Leaf samples were collected from the upper portion of each sampled tree crown using an arborist slingshot. Sampling was conducted at three predefined crown aspects—north, southeast, and southwest—to obtain spatially distributed samples from different portions of the crown rather than relying on a single crown position. For each tree and sampling campaign, 150 leaves were collected, with 50 leaves obtained from each aspect. The same three-aspect sampling design was applied consistently across trees, sites, and campaigns. Leaves were not classified as exclusively sunlit or shaded during collection; consequently, no distinction between sunlit and shaded foliage was made in the subsequent analysis.

The 50 leaves collected from each crown aspect were treated as one sampling unit, and their chlorophyll measurements were averaged to obtain an aspect-specific chlorophyll observation. Relative chlorophyll status was measured in situ using a Konica Minolta SPAD-502 chlorophyll meter (Konica Minolta, Inc., Tokyo, Japan; accuracy ±1 SPAD unit).

For each leaf, three SPAD readings were taken away from the main veins and visible OLB egg clusters and averaged. The resulting SPAD values were converted to leaf chlorophyll content (LCC; $\mu g\ cm^{-2}$) using the species-specific calibration relationship developed for pedunculate oak (*Quercus robur*) by Brown et al. [49]:

$$LCC = 0.1719e^{0.0355\,SPAD} \quad (1)$$

where SPAD represents the measured SPAD-502 reading and LCC represents the corresponding field-calibrated LCC in $\mu g\ cm^{-2}$. Thus, the LCC values used in subsequent CCC calculations were not uncalibrated SPAD readings, but chlorophyll-content estimates obtained using a published species-specific calibration. The same conversion was applied at both sites.

The fundamental observational unit used for regression modeling was a crown-aspect observation, defined by one tree, one crown aspect, one sampling month, and one year. Each observation paired the mean field-calibrated LCC from the 50 leaves sampled within a given crown aspect with UAV reflectance extracted from the corresponding crown-aspect polygon. Three crown-aspect observations were therefore generated for each sampled tree and campaign, except where an observation was removed because of invalid data. Table 1 reports the number of unique trees and corresponding crown-aspect observations for each year, site, and sampling month. Because multiple crown-aspect observations originated from the same tree, tree identity was used as the grouping variable in cross-validation, as described in Section 2.3.1.

Table 1. Number of unique trees and crown-aspect observations by year, site, and sampling month.

Year	Site	Month	Unique Trees (n)	Crown-Aspect Observations (N)
2021	A	May	23	69
	A	July	23	69
	A	September	30	90
2022	A	May	30	90
	A	July	30	90
	A	September	30	89
	B	May	30	90
	B	July	30	90
	B	September	30	90
2023	A	May	30	90
	A	July	30	90
	A	September	30	90
	B	July	30	90

Leaf area index (LAI) was estimated from the UAV-derived normalized difference red-edge index (NDRE) and photogrammetrically derived CHM using the empirical relationship reported by [50]:

$$LAI = 1.84 + 0.53(NDRE \times CHM) \quad (2)$$

where NDRE was calculated from the red-edge and near-infrared Parrot Sequoia bands and CHM represents the photogrammetrically derived relative canopy height. The relationship was applied to the corresponding crown-aspect UAV observations to estimate LAI for the sampled crown areas. The published relationship was adopted directly and was not recalibrated or independently validated using field LAI measurements at the study sites. LAI is therefore referred to hereafter as UAV-estimated LAI rather than field-measured LAI.

Because CHM contributes to this relationship, uncertainty associated with photogrammetric terrain reconstruction may propagate into UAV-estimated LAI and subsequently into derived CCC. This limitation is considered further in Section 4.4.

Canopy chlorophyll content (CCC) was subsequently calculated for each crown-aspect observation as:

$$CCC = LCC \times LAI \quad (3)$$

where LCC represents field-calibrated LCC and LAI represents UAV-estimated LAI. CCC therefore represents a derived canopy-level chlorophyll metric rather than a directly field-measured variable. The resulting derived CCC value was assigned to the corresponding crown-aspect observation and used as the response variable in the regression analyses. LCC represents chlorophyll content per unit leaf area ($\mu g\ cm^{-2}$ leaf area), whereas CCC represents chlorophyll content per unit ground area ($\mu g\ cm^{-2}$ ground area). Because LAI expresses leaf area per unit ground area, multiplying LCC by LAI converts the leaf-level quantity into a canopy-level quantity. Accordingly, CCC values may exceed typical leaf-level chlorophyll concentrations and should not be directly compared with LCC ranges.

The same trees were revisited across campaigns from 2021 to 2023. Models were developed separately for each site and sampling month; therefore, May, July, and September represented separate retrieval problems corresponding to different phenological and acquisition conditions rather than sequential models used to predict temporal change.

For clarity, the response variable throughout the retrieval analysis was derived CCC, calculated as the product of field-calibrated LCC and UAV-estimated LAI. The empirical predictor variables consisted exclusively of reflectance in the four Parrot Sequoia bands (green, red, red edge, and near-infrared); NDRE, CHM, and LAI were not included as additional empirical predictors. However, because NDRE was calculated from two of these UAV bands and contributed to UAV-estimated LAI, the derived CCC response variable is not fully independent of the empirical predictor space. This partial dependence is considered explicitly when interpreting empirical model performance in Section 4.4. For the hybrid approach, PROSAIL-simulated spectra were resampled to the same four Parrot Sequoia bands and used within the PROSAIL–GPR framework described in Section 2.3.2.

Hereafter, the terms field-calibrated LCC, UAV-estimated LAI, derived CCC, and predicted CCC are used consistently to distinguish the origin and role of these variables.

2.3. Regression Modeling

Two complementary approaches were evaluated for canopy chlorophyll content (CCC) retrieval: (1) empirical machine-learning regression and (2) a hybrid radiative transfer model–machine learning (RTM–ML) framework. The empirical analysis evaluated six regression algorithms, whereas the hybrid analysis focused on a specific PROSAIL–GPR implementation. GPR provided a common regression framework for direct comparison between the empirical and hybrid approaches, thereby reducing differences attributable to the regression algorithm itself. The hybrid analysis was therefore designed to evaluate the tested PROSAIL–GPR framework rather than all possible combinations of radiative transfer models and machine-learning algorithms.

The two approaches differed primarily in the source of information used to establish the relationship between spectral reflectance and CCC. The empirical models learned this relationship directly from the crown-aspect UAV reflectance and corresponding derived CCC observations, whereas the hybrid GPR was trained on PROSAIL-simulated spectral–biophysical relationships, with active learning informed only by observations from the training trees within each cross-validation fold, as described in Section 2.3.2. The comparison therefore evaluated whether the tested PROSAIL-based physical constraint pro-

vided an advantage over observation-based empirical retrieval under the same four-band spectral configuration and tree-grouped validation framework.

Regression modeling was implemented using the Automated Radiative Transfer Models Operator (ARTMO, version 3.33), a MATLAB-based environment for radiative transfer modeling, spectral analysis, and machine-learning regression across the optical domain (400–2500 nm) (MATLAB R2020a, The MathWorks, Inc., Natick, MA, USA). ARTMO integrates radiative transfer models, including PROSAIL, with machine-learning regression algorithms and was used to support the empirical and hybrid retrieval workflows [30].

2.3.1. Empirical Machine-Learning Regression

Six regression algorithms representing different modeling strategies were evaluated: least-squares linear regression (LSLR), kernel ridge regression (KRR), regression tree (RT), random forest (RF), neural network (NN), and Gaussian process regression (GPR) (Table 2). These algorithms represent linear, kernel-based, tree-based, ensemble, neural-network, and probabilistic regression approaches, respectively, and were used to characterize empirical CCC retrieval performance from the four-band UAV observations.

Table 2. Machine-learning regression algorithms, hyperparameter configurations, and optimization procedures used for empirical CCC retrieval.

Algorithm	Hyperparameters and Optimization	Reference
Least Squares Linear Regression (LSLR)	No tunable hyperparameters; coefficients for the four reflectance bands were estimated by least squares.	[51]
Kernel Ridge Regression (KRR)	RBF kernel; kernel width $\sigma = 1.66$ and regularization $\gamma = 0.014$, selected by grid search over $\sigma = 0.1$–10 and $\gamma = 10^{-6}$–1 using cross-validation within the training data.	[52]
Regression Trees (RT)	Minimum leaf size = 1, minimum parent size = 10, with pruning enabled.	[53]
Random Forest (RF)	200 trees; minimum leaf size = 5; all four bands available at each split; out-of-bag prediction enabled.	[54]
Neural Networks (NN)	One hidden layer with nine neurons (tansig) and linear output; scaled conjugate-gradient training; mean squared error objective; maximum 100 epochs.	[55]
Gaussian Process Regression (GPR)	ARD rational quadratic kernel; kernel length scales, signal variance, shape parameter, and noise variance estimated by maximizing marginal likelihood within the training data using quasi-Newton optimization.	[56]

Models were developed independently for each site and sampling month. Within each site × month combination, observations from the corresponding month were pooled across the available years (2021–2023). Thus, May, July, and September constituted separate retrieval problems, and observations were not pooled among sampling months or between Sites A and B. This design allowed each model to represent site- and phenological-stage-specific relationships between UAV reflectance and derived CCC, rather than assuming that a single relationship was transferable across sites or sampling periods.

The predictor variables consisted exclusively of reflectance in the four Parrot Sequoia bands (green, red, red edge, and near-infrared) extracted from each crown-aspect polygon. NDRE, CHM, and UAV-estimated LAI were not included as additional empirical predictor variables. Reflectance spectra from non-vegetated soil surfaces, identified in the UAV imagery using the LabelMe tool in ARTMO, were also included and assigned CCC = 0 to extend the modeled spectral–CCC domain toward non-vegetated conditions. A total of 28, 28, and 30 soil spectra were included for Site A and 10, 20, and 20 for Site B in May, July, and September, respectively. Because the soil spectra were not associated with individual trees, they were used only to augment the training data within each cross-validation fold and were not included among the held-out tree observations used to calculate validation performance.

Each biological observation used for regression modeling corresponded to one crown aspect of a sampled tree within a specific month and year. The four-band UAV reflectance extracted from each manually delineated crown-aspect polygon was paired with the derived CCC value for the corresponding crown aspect, as described in Section 2.2. Crown-aspect observations were retained as individual modeling observations and were not averaged to produce one observation per tree.

Model performance was evaluated using three-fold tree-grouped cross-validation to account for the non-independence of crown-aspect observations originating from the same tree. Tree identity was used as the grouping variable, and all crown-aspect observations associated with a given physical tree were assigned to the same fold. For trees sampled repeatedly across years, observations from the same tree were retained within the same fold. Within each site × month dataset, two tree groups were used for model training and the remaining group for validation, with the procedure repeated until each group had served once as the validation fold. Consequently, no crown-aspect observation or repeated-year observation from a held-out tree occurred in the corresponding training subset. This design evaluates generalization to held-out trees within the sampled sites and campaigns while retaining crown aspects as the fundamental spectral observational units.

The same tree-grouped fold assignments were subsequently used to evaluate the hybrid PROSAIL–GPR approach (Section 2.3.2), allowing the empirical and hybrid approaches to be evaluated using the same held-out trees.

Model performance was quantified using root mean square error (RMSE), normalized root mean square error (NRMSE), and the coefficient of determination (R^2). R^2 was calculated from the residual and total sums of squares as $R^2 = 1 - SS_{res}/SS_{tot}$ and therefore represents predictive goodness of fit; it was not calculated as the square of Pearson's correlation coefficient. RMSE quantified prediction error in the original CCC units, whereas NRMSE expressed RMSE relative to the maximum derived CCC for the corresponding site and sampling month:

$$\mathrm{NRMSE}(\%) = 100 \times \frac{\mathrm{RMSE}}{\mathrm{CCC}_{max}} \quad (4)$$

where CCC_{max} is the maximum derived CCC for the corresponding site and sampling month. This normalization expresses prediction error relative to the maximum CCC represented within each dataset and facilitates comparison among sites and sampling periods with different CCC magnitudes.

For the observed-versus-predicted plots, Pearson's correlation coefficient (R) was additionally calculated to describe the strength of the linear association between derived and predicted CCC. Pearson's R was used as a descriptive measure for these plots and was not treated as equivalent to the predictive R^2 reported for model performance.

The algorithms were implemented using the ARTMO machine-learning regression toolbox (MLRA), with the configurations summarized in Table 2. Reflectance predictors were standardized to zero mean and unit variance using parameters estimated exclusively

from the training data within each cross-validation fold and subsequently applied to the corresponding held-out observations. GPR used an automatic relevance determination (ARD) rational quadratic kernel, with hyperparameters estimated by maximizing the marginal likelihood. KRR used a radial basis function (RBF) kernel, with kernel width and regularization selected through internal cross-validation using the training data. RF was implemented using MATLAB TreeBagger, and RT used a single regression tree. NN used a feedforward architecture, while LSLR required no tunable hyperparameters. Model-specific settings and optimization procedures are reported in Table 2 to facilitate reproducibility.

Although all six algorithms were evaluated to characterize empirical retrieval performance, GPR was retained as the common empirical reference model for detailed derived-versus-predicted comparisons, spatial mapping, and direct comparison with the hybrid PROSAIL–GPR implementation (Table 2). This selection does not imply that GPR was the highest-performing empirical algorithm for every site × month combination. Rather, retaining the same regression algorithm on both sides of the empirical–hybrid comparison reduces algorithm choice as a source of variation and allows the effect of the different training frameworks to be examined more directly.

2.3.2. Hybrid PROSAIL–GPR Approach

GPR was selected as the regression algorithm for the hybrid framework to provide a common regression basis for comparison with empirical GPR and because of its compatibility with the iterative active-learning procedure used to optimize the PROSAIL simulation space. The objective of the hybrid analysis was not to compare all possible combinations of radiative transfer models and machine-learning algorithms, but to evaluate a specific PROSAIL–GPR implementation under the same spectral and validation conditions as the empirical retrieval. Using GPR in both frameworks reduced variation attributable to the choice of regression algorithm and facilitated comparison between observation-based empirical retrieval and the tested simulation-based hybrid framework.

The hybrid approach combined the PROSAIL radiative transfer model with GPR within ARTMO. PROSAIL couples the PROSPECT-4 leaf optical model with the 4SAIL canopy bidirectional reflectance model to simulate canopy reflectance as a function of biochemical, structural, soil, and illumination parameters. Rather than directly inverting PROSAIL against the UAV observations, look-up tables (LUTs) of simulated canopy spectra were generated across the parameter ranges listed in Table 3.

The Cab and LAI simulation ranges were defined to encompass the complete ranges represented in the study dataset and to avoid imposing different Cab domains on the two sites. Across sites and sampling periods, field-derived LCC ranged from 20.13 to 123.73 μg cm^{-2} and UAV-estimated LAI from 0.73 to 8.11 m^2 m^{-2}. Common simulation ranges of Cab = 10–130 μg cm^{-2} and LAI = 0.5–8.5 m^2 m^{-2} were therefore applied at both sites, providing margins beyond the observed and estimated ranges. The remaining PROSAIL parameters were constrained using published ranges [32–34] and acquisition- and site-specific information, as applicable (Table 3).

To examine whether the specification of the PROSAIL parameter domain influenced hybrid retrieval performance, two LUT parameterizations were evaluated. The first used the a priori PROSAIL parameter ranges specified in Table 3. In the second, the Cab and LAI ranges were adjusted within each cross-validation fold to encompass the corresponding ranges represented by the training trees only. Observations from held-out validation trees were not used to define these training-tree-informed ranges. The subsequent active-learning and LUT-selection procedures were conducted independently for each parameterization and within each training fold. This comparison was used to assess the sensitivity of hybrid

retrieval to Cab and LAI parameter-range specification rather than to select parameter ranges using validation observations.

Table 3. Input variables and parameter ranges used in the PROSPECT-4 and 4SAIL simulations.

Model	Parameter	Unit	Site A	Site B
PROSPECT-4	Leaf structure (N)	–	1–2	1.5–2.5
	Chlorophyll content (Cab)	$\mu g\ cm^{-2}$	10–130	10–130
	Leaf water content (Cw)	$g\ cm^{-2}$	0.006–0.018	0.008–0.020
	Dry matter content (Cm)	$g\ cm^{-2}$	0.006–0.020	0.005–0.018
4SAIL	Leaf Area Index (LAI)	$m^2\ m^{-2}$	0.5–8.5	0.5–8.5
	Hotspot parameter	–	0.0015–0.006	0.0015–0.006
	Mean leaf angle	°	20–40	20–40
	Solar zenith angle	°	33–51	34–55
	Diffuse radiation fraction	%	25–55	25–55
	Observer zenith angle	°	0–10	0–10
	Soil brightness coefficient	–	0.10–0.25	0.10–0.40
	Relative azimuth angle	°	123–142	122–142

PROSAIL simulations were spectrally resampled to the four Parrot Sequoia bands using the sensor-specific spectral response functions. Thus, the empirical and hybrid retrievals were based on the same four-band spectral representation, avoiding an information advantage for the hybrid approach arising from the full spectral resolution of the PROSAIL simulations.

Initial LUT sampling was performed using Latin hypercube sampling with 1000 PROSAIL simulations. Each simulation represented a combination of the biochemical, structural, soil, and illumination parameters listed in Table 3 and the corresponding PROSAIL-simulated canopy reflectance. Cab was therefore an input parameter to the PROSAIL simulations, whereas the derived CCC observations used in model evaluation were not independently simulated PROSAIL input parameters.

Active learning (AL) was subsequently applied using Euclidean distance-based diversity (EBD) and GPR to reduce the initial simulation space and retain simulations most relevant to the observed training domain. AL was conducted separately for each site and sampling month and independently within each tree-grouped cross-validation fold.

Within each fold, only UAV reflectance and corresponding derived CCC observations from the training trees were available to inform the AL procedure. Candidate reduced LUTs containing different numbers of retained PROSAIL simulations were evaluated using the training observations, and the number of simulations producing the lowest RMSE against the training-tree derived CCC was retained. Thus, derived CCC from the training trees contributed observational information to optimization of the simulated training space through AL; it was not treated as an independently simulated PROSAIL input parameter. Neither UAV reflectance nor derived CCC from the held-out validation trees was used during active learning or LUT selection.

The resulting reduced, fold-specific PROSAIL simulation set was subsequently used for hybrid GPR model development. Neither UAV reflectance nor derived CCC observations from trees assigned to the validation fold were used for AL, LUT selection, or model development. The trained hybrid GPR was then applied to UAV reflectance observations from the held-out trees, and predicted CCC was evaluated against the corresponding derived CCC observations. This procedure was repeated independently for all three folds. Consequently, each fold used an independently optimized simulation subset rather than a LUT optimized using the complete observational dataset.

As in the empirical analysis, soil spectra representing non-vegetated surfaces were assigned CCC = 0 and included to extend the spectral domain toward non-vegetated conditions. Because the soil spectra were not associated with individual trees, they were used only to augment the training data within each cross-validation fold and were not included among the held-out tree observations used to calculate validation performance.

The hybrid approach should therefore not be interpreted as being developed independently of the observational data. Although the initial spectral space was generated from PROSAIL simulations, UAV reflectance and derived CCC observations from the training trees informed the AL-based selection of the relevant subset of simulations. The tree-grouped validation design nevertheless ensured that information from held-out trees did not contribute to active learning, LUT selection, or hybrid model development.

The iterative AL procedure and hybrid GPR modeling were implemented in MATLAB R2020a. GPR was used within the AL framework because it provided a computationally practical nonlinear regression method for repeated evaluation of candidate simulation subsets. The same tree-grouped fold assignments were used for the empirical and hybrid approaches, allowing their performance to be evaluated against the same held-out trees using R^2, RMSE, and NRMSE.

A schematic of the complete workflow, from UAV image processing and crown-aspect spectral extraction through empirical machine-learning and hybrid PROSAIL–GPR modeling to tree-grouped model evaluation and CCC prediction, is presented in Figure 2.

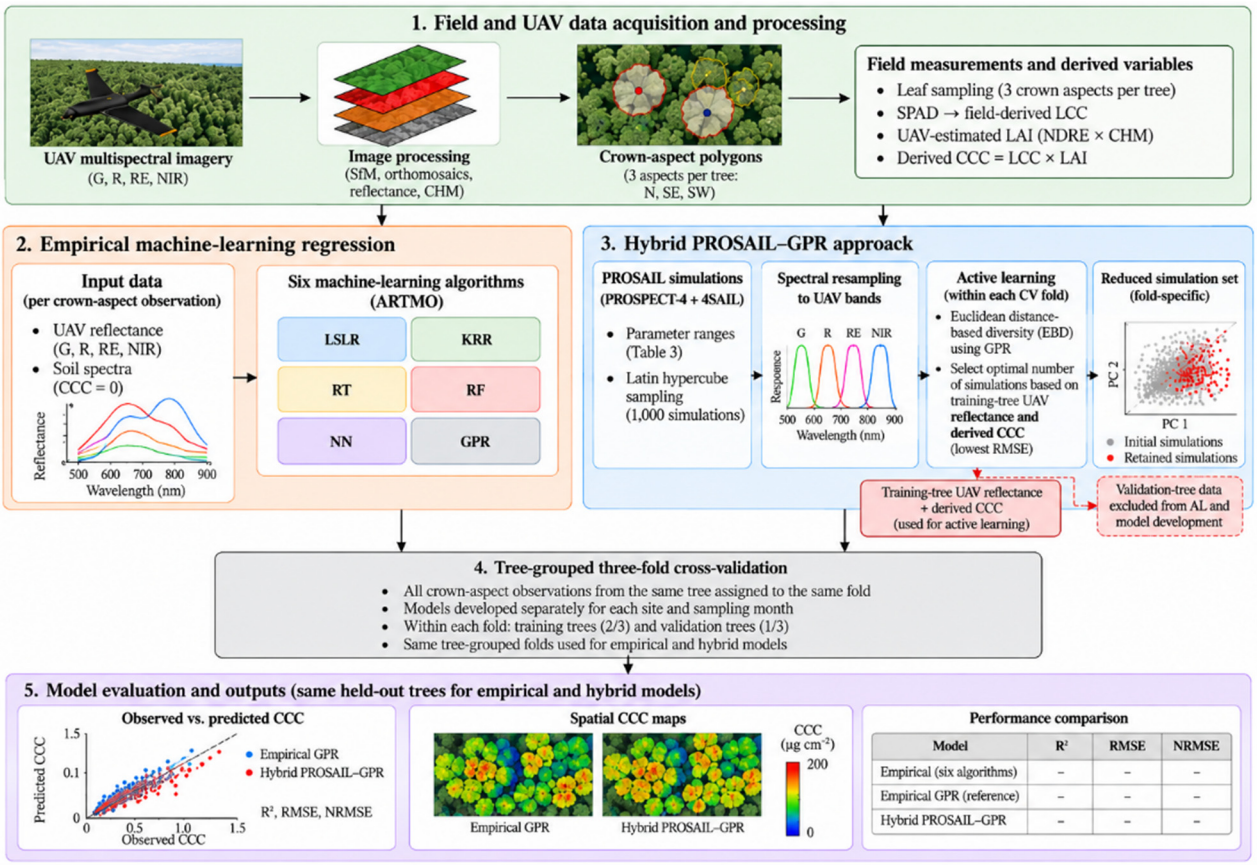


Figure 2. Workflow for canopy chlorophyll content (CCC) retrieval, showing UAV data processing and crown-aspect spectral extraction, empirical machine-learning regression, hybrid PROSAIL–GPR modeling with fold-specific active learning, and tree-grouped three-fold cross-validation.

3. Results

3.1. Variation in Leaf Chlorophyll, LAI, and Canopy Chlorophyll

Field-derived leaf chlorophyll content (LCC) and UAV-estimated leaf area index (LAI) were used to calculate derived canopy chlorophyll content (CCC) across the three sampling periods (Table 4). The descriptive statistics in Table 4 are based on crown-aspect observations, with each sampled tree generally contributing three observations per campaign. The numbers of unique trees and crown-aspect observations are reported separately to distinguish the biological sampling units from the crown-aspect observations used in the retrieval analysis.

Table 4. Descriptive statistics of field-derived leaf chlorophyll content (LCC), UAV-estimated leaf area index (LAI), and derived canopy chlorophyll content per unit ground area (CCC) at Sites A and B across the three sampling periods.

Month	Site	Tree Records (n)	Obs. (N)	LCC (μg cm^{-2})				LAI (m^2 m^{-2})				CCC (μg cm^{-2})			
				Mean	SD	Min	Max	Mean	SD	Min	Max	Mean	SD	Min	Max
May	A	83	249	48.02	13.38	20.13	84.33	2.71	0.46	1.91	4.57	130.60	42.08	41.19	248.71
	B	30	90	53.35	8.38	34.84	69.62	3.71	1.22	2.23	7.86	200.86	82.23	84.14	484.71
July	A	83	249	53.01	12.70	24.26	86.76	2.97	0.60	1.98	5.45	159.06	54.14	51.93	363.88
	B	60	180	60.70	15.08	34.96	101.79	3.47	1.14	2.07	7.64	213.09	93.04	77.03	529.85
September	A	90	269	53.31	13.43	23.16	123.73	2.98	0.92	0.73	8.11	160.06	61.32	18.57	456.26
	B	30	90	53.02	14.12	29.59	84.03	2.84	0.87	1.70	6.80	157.44	86.19	51.54	551.15

At Site A, mean field-derived LCC increased from 48.02 ± 13.38 μg cm^{-2} in May to 53.01 ± 12.70 μg cm^{-2} in July and remained similar in September (53.31 ± 13.43 μg cm^{-2}). At Site B, mean LCC increased from 53.35 ± 8.38 μg cm^{-2} in May to 60.70 ± 15.08 μg cm^{-2} in July and decreased to 53.02 ± 14.12 μg cm^{-2} in September.

UAV-estimated LAI showed a somewhat different pattern. At Site A, mean LAI increased from 2.71 ± 0.46 m^2 m^{-2} in May to 2.97 ± 0.60 m^2 m^{-2} in July and remained similar in September (2.98 ± 0.92 m^2 m^{-2}). At Site B, mean LAI was 3.71 ± 1.22 m^2 m^{-2} in May, 3.47 ± 1.14 m^2 m^{-2} in July, and 2.84 ± 0.87 m^2 m^{-2} in September. The difference between the May and July means at Site B should not be interpreted as a direct within-year phenological decline because the pooled monthly datasets differed in campaign composition: May represented one annual campaign, whereas July included two annual campaigns.

Derived CCC at Site A increased from 130.60 ± 42.08 μg cm^{-2} in May to 159.06 ± 54.14 μg cm^{-2} in July and remained similar in September (160.06 ± 61.32 μg cm^{-2}). At Site B, mean derived CCC was 200.86 ± 82.23 μg cm^{-2} in May and 213.09 ± 93.04 μg cm^{-2} in July, decreasing to 157.44 ± 86.19 μg cm^{-2} in September. These site-level differences are descriptive and should not be interpreted as effects of OLB pressure because the two sites also differed in geographic location and associated environmental conditions.

As an additional check on the influence of repeated crown-aspect observations, aggregation of the three crown aspects to the tree level had little effect on the central tendency of UAV-estimated LAI or derived CCC. Mean values were essentially unchanged across site × month combinations. In particular, the higher mean UAV-estimated LAI at Site B in May than in July (3.71 versus 3.47 m^2 m^{-2}) was retained after tree-level aggregation, indicating that this pattern was not produced by treating crown aspects as independent observations. The retrieval analyses nevertheless retained crown-aspect observations as the spectral observational units, while accounting for their within-tree dependence through tree-grouped cross-validation (Section 2.3.1).

3.2. CCC Retrieval Using Empirical Machine Learning

3.2.1. Comparative Performance of Empirical Models

Six empirical machine-learning regression algorithms were evaluated for CCC retrieval across the two sites and three sampling periods. Models were developed independently for May, July, and September at each site by pooling observations from the corresponding campaigns across the available years. Crown-aspect observations were retained as individual modeling observations, while all observations belonging to the same tree, including repeated observations across years where applicable, were assigned to the same cross-validation fold. Thus, the reported performance statistics represent prediction for held-out trees rather than random observation-level validation.

Tree-grouped three-fold cross-validation produced moderate retrieval performance and revealed variation among algorithms, sites, and sampling periods (Table 5). At Site A, GPR provided the strongest performance in May ($R^2 = 0.61$, RMSE = 27.04 μg cm^{-2}, NRMSE = 10.87%) and the lowest prediction error in July (RMSE = 44.28 μg cm^{-2}, NRMSE = 12.17%, $R^2 = 0.38$). In September, RF provided the strongest overall performance ($R^2 = 0.34$, RMSE = 50.60 μg cm^{-2}, NRMSE = 11.09%).

Table 5. Performance of empirical machine-learning models for CCC retrieval using tree-grouped three-fold cross-validation. The lowest RMSE and NRMSE and highest R^2 for each site × month combination are indicated in bold.

Month		SITE A			SITE B		
		RMSE (μg cm^{-2})	**NRMSE (%)**	**R^2**	**RMSE (μg cm^{-2})**	**NRMSE (%)**	**R^2**
May	GPR	**27.04**	**10.87**	**0.61**	89.04	18.37	0.32
	KRR	27.99	11.26	0.57	75.64	15.61	0.30
	RF	27.86	11.20	0.59	**74.83**	**15.44**	0.32
	NN	29.93	12.04	0.57	126.77	26.15	0.18
	RT	34.44	13.85	0.42	83.21	17.17	0.20
	LSLR	29.38	11.81	0.58	79.33	16.37	**0.33**
July	GPR	**44.28**	**12.17**	**0.38**	76.18	14.38	0.47
	KRR	45.38	12.47	0.37	81.22	15.33	0.40
	RF	46.92	12.89	0.34	69.71	13.16	**0.60**
	NN	49.06	13.48	0.38	92.46	17.45	0.35
	RT	53.55	14.72	0.27	88.66	16.73	0.45
	LSLR	46.08	12.66	0.35	**65.28**	**12.32**	0.56
September	GPR	51.70	11.33	0.31	78.37	14.22	0.41
	KRR	51.47	11.28	0.31	71.84	13.04	**0.57**
	RF	**50.60**	**11.09**	**0.34**	**67.07**	**12.17**	0.52
	NN	53.27	11.68	0.32	73.71	13.37	0.32
	RT	60.35	13.23	0.20	88.45	16.05	0.42
	LSLR	51.49	11.29	0.29	75.08	13.62	0.48

Note: Crown-aspect observations were retained as individual modeling observations, but all observations belonging to the same tree, including repeated observations across years where applicable, were assigned to the same cross-validation fold. Thus, observations from a held-out tree did not contribute to model training.

At Site B, no single algorithm consistently performed best across sampling periods. In May, RF produced the lowest RMSE (74.83 μg cm^{-2}; NRMSE = 15.44%), whereas LSLR produced the highest R^2 (0.33). In July, LSLR produced the lowest RMSE (65.28 μg cm^{-2}; NRMSE = 12.32%), whereas RF achieved the highest R^2 (0.60). In September, RF produced the lowest RMSE (67.07 μg cm^{-2}; NRMSE = 12.17%), whereas KRR achieved the highest R^2 (0.57).

Performance also differed between sites and sampling periods. Prediction errors were lower at Site A than at Site B in May, whereas Site B generally showed higher R^2 values in July and September. Overall, the tree-grouped results demonstrate that empirical CCC retrieval performance depended on site, sampling period, and regression algorithm, with no single algorithm consistently providing the best performance across all six site × month combinations.

Because model rankings varied among site × month combinations, GPR was retained as a common empirical reference model for subsequent derived-versus-predicted comparisons and spatial CCC visualization. This provided a consistent regression framework across sites and sampling periods and enabled direct comparison with the hybrid PROSAIL–GPR implementation; selection of GPR for these analyses does not imply that it was the highest-performing empirical algorithm in every site × month combination.

3.2.2. Agreement Between Derived and Predicted CCC

Because no single empirical algorithm was consistently optimal across all site × month combinations, GPR was retained as the common empirical reference model for detailed derived-versus-predicted comparisons (Figure 3). This provided a consistent basis for visualization across sites and sampling periods and enabled direct comparison with the hybrid PROSAIL–GPR approach; selection of GPR for these plots does not indicate that it was the highest-performing empirical algorithm in every site × month combination.

Pearson correlation analysis showed positive but variable associations between derived and predicted CCC for the empirical GPR models (Figure 3). At Site A, Pearson correlation coefficients (R) were 0.76, 0.58, and 0.55 for May, July, and September, respectively. At Site B, R was 0.34 in May, 0.60 in July, and 0.50 in September.

Pearson R was used to characterize the strength of the linear association between derived and predicted CCC and is complementary to, rather than equivalent to, the predictive R^2 reported in Table 5. The R^2 values in Table 5 quantify predictive goodness of fit from the residual and total sums of squares, whereas Pearson R quantifies linear association between derived and predicted values. The 1:1 line in Figure 3 is provided only as a visual reference for agreement and does not represent a fitted regression. Predictive performance was therefore evaluated primarily using the tree-grouped cross-validated R^2, RMSE, and NRMSE reported in Table 5, with Pearson R providing an additional description of association.

The derived-versus-predicted relationships varied among sites and sampling periods, with Pearson R ranging from 0.34 to 0.76. The strongest empirical GPR association occurred at Site A in May ($R = 0.76$), whereas the weakest occurred at Site B in May ($R = 0.34$). These association measures should be interpreted together with, rather than as substitutes for, the cross-validated predictive metrics in Table 5. In particular, differences between Pearson R and predictive R^2 emphasize that linear association between derived and predicted CCC does not necessarily indicate equivalent agreement in prediction magnitude.

3.2.3. Spatial Retrieval of CCC

Spatial predictions from the empirical GPR models revealed fine-scale variation in retrieved CCC within the two forest stands (Figure 4). GPR was retained as the common empirical model for spatial visualization to provide a consistent comparison across sites and sampling periods and with the hybrid PROSAIL–GPR approach, rather than because it was the highest-performing empirical algorithm for every site × month combination.

Site A exhibited pronounced spatial heterogeneity in predicted CCC, with contiguous areas of relatively low and high values, whereas Site B generally exhibited higher predicted CCC. The spatial patterns indicate that the four-band UAV imagery combined with empirical GPR resolved spatial variation in the derived CCC metric within the studied stands at

the scale represented by the UAV observations. However, these patterns should not be interpreted as direct maps of OLB infestation or damage severity because pest abundance and damage severity were not quantitatively measured. The maps therefore represent spatial variation in retrieved CCC rather than a direct assessment of forest-health status.

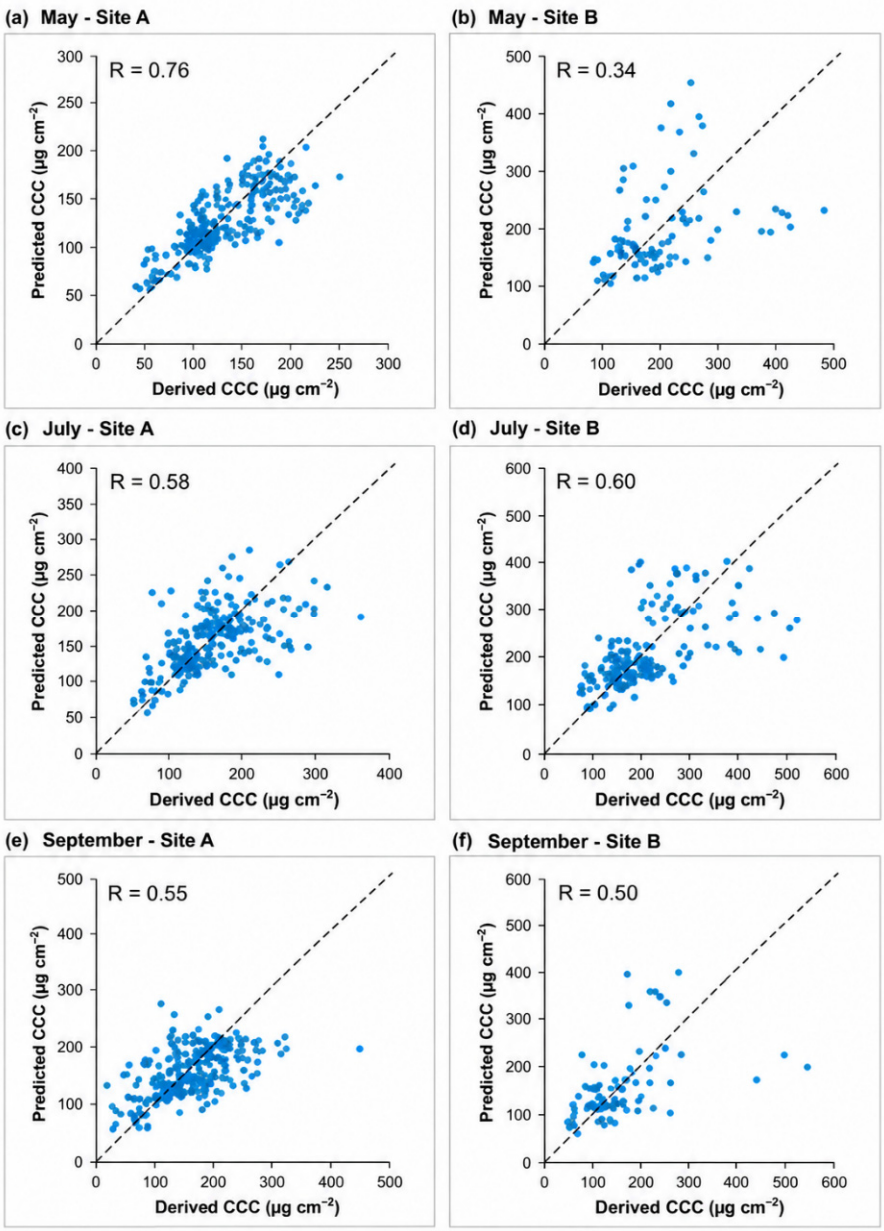


Figure 3. Relationships between derived and predicted canopy chlorophyll content per unit ground area (CCC) for the empirical GPR models under tree-grouped three-fold cross-validation across sites and sampling periods. GPR is presented as a common empirical reference model for visualization and comparison with the hybrid PROSAIL–GPR approach. Pearson R describes the linear association between derived and predicted CCC; predictive R^2, RMSE, and NRMSE are reported in Table 5. The dashed line represents the 1:1 relationship and is provided as a visual reference for agreement rather than as a fitted regression.

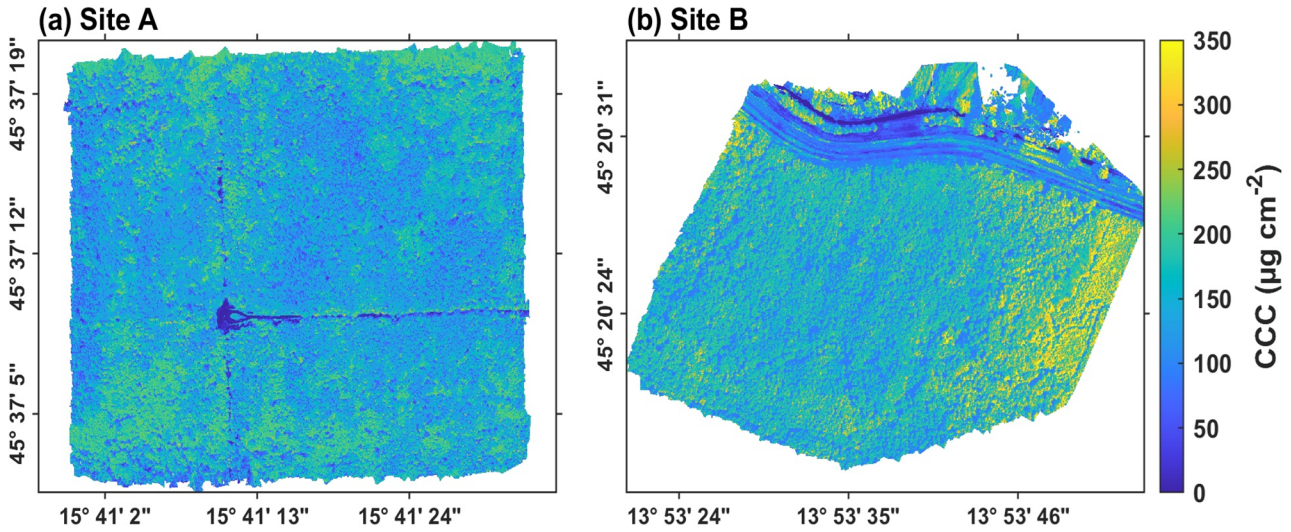


Figure 4. Spatial distribution of canopy chlorophyll content per unit ground area (CCC) predicted using the empirical GPR models for July 2022 at (**a**) Site A and (**b**) Site B. GPR was used as a common empirical reference model for spatial visualization and comparison across sites and sampling periods; comparative predictive performance of all six empirical algorithms is reported in Table 5. The maps represent retrieved CCC and should not be interpreted as direct estimates of oak lace bug infestation or damage severity.

3.3. Hybrid PROSAIL–GPR Retrieval

The hybrid PROSAIL–GPR approach was evaluated using the same tree-grouped three-fold cross-validation framework as the empirical models, with active learning (AL) and LUT optimization repeated independently within each training fold. UAV reflectance and derived CCC from held-out trees were excluded from AL, LUT selection, and model development. Two LUT parameterizations were evaluated: the original a priori PROSAIL parameter ranges and training-tree-informed ranges in which the Cab and LAI ranges were adjusted using information from the training trees (Table 6).

Hybrid retrieval performance varied substantially among sites, sampling periods, and LUT parameterizations (Table 6). Using the original PROSAIL parameter ranges, R^2 ranged from 0.05 to 0.15 across the six site × month combinations, while NRMSE ranged from 24.34% to 55.55%. The training-tree-informed parameterization did not produce a consistent improvement, with R^2 ranging from 0.00 to 0.20 and NRMSE from 20.23% to 106.31%. Thus, adjusting the Cab and LAI ranges using information from the training trees did not systematically improve hybrid retrieval relative to the original parameterization.

The number of simulations retained through AL also varied considerably among folds, ranging from 100 to 1000 simulations under the original parameterization and from 100 to 975 under the training-tree-informed parameterization. This variation indicates that the subset of PROSAIL simulations selected as most relevant to the training observations was fold-dependent. Because AL and LUT optimization were conducted independently within each training fold, information from the held-out trees did not contribute to selection of the simulation subset used to develop the corresponding hybrid model.

Compared with the empirical models (Table 5), the hybrid PROSAIL–GPR approach generally produced higher prediction errors and lower R^2 values under the same tree-grouped validation framework. The tested hybrid approach did not outperform the corresponding empirical GPR model in predictive R^2, RMSE, or NRMSE for any site × month combination under either LUT parameterization. The magnitude of the difference varied among sites, sampling periods, and LUT parameterizations.

Table 6. Performance of the hybrid PROSAIL–GPR approach under tree-grouped three-fold cross-validation using two LUT parameterizations. Active learning (AL) and LUT optimization were repeated independently within each training fold, and UAV reflectance and derived CCC from held-out trees were excluded from AL, LUT selection, and model development. Performance metrics represent the means of the three fold-specific validation results.

Month	Site	LUT Parameterization	Simulations Retained After AL			RMSE ($\mu g\ cm^{-2}$)	NRMSE (%)	R^2
			Fold 1	Fold 2	Fold 3			
May	A	Original parameter ranges	1000	100	200	138.16	55.55	0.05
	A	Training-tree-informed ranges	225	100	100	264.41	106.31	0.03
	B	Original parameter ranges	100	100	425	190.45	39.29	0.09
	B	Training-tree-informed ranges	950	100	100	128.48	26.51	0.15
July	A	Original parameter ranges	100	400	125	135.49	37.23	0.13
	A	Training-tree-informed ranges	975	775	475	111.33	30.59	0.03
	B	Original parameter ranges	100	150	125	268.65	50.70	0.11
	B	Training-tree-informed ranges	150	100	100	301.28	56.86	0.06
September	A	Original parameter ranges	200	100	100	118.49	25.97	0.14
	A	Training-tree-informed ranges	225	625	225	123.59	27.09	0.00
	B	Original parameter ranges	300	125	150	134.14	24.34	0.15
	B	Training-tree-informed ranges	950	625	250	111.48	20.23	0.20

Note: Original parameter ranges refer to the a priori PROSAIL parameterization specified in Table 3. Training-tree-informed ranges refer to the alternative parameterization in which Cab and LAI ranges were adjusted using information from the training trees within each fold. AL was repeated independently within each training fold, and candidate reduced LUTs were evaluated using UAV reflectance and derived CCC from the training trees. The number of retained simulations was selected based on the lowest training-tree RMSE for derived CCC. UAV reflectance and derived CCC from held-out trees were excluded from AL, LUT selection, and model development. AL = active learning; LUT = look-up table; GPR = Gaussian process regression.

Derived-versus-predicted relationships for the hybrid models also varied substantially among sites and sampling periods (Figure 5). Pearson R values were 0.51, 0.37, and 0.27 at Site A in May, July, and September, respectively, and 0.26, 0.65, and −0.14 at Site B. Thus, the strength of linear association varied markedly among site × month combinations, from essentially no association at Site B in September ($R = -0.14$) to the highest association at Site B in July ($R = 0.65$). Predictions also frequently deviated from the 1:1 relationship, with the magnitude and direction of prediction errors varying among site × month combinations. In some cases, predicted CCC extended beyond the range represented by the derived CCC values, further indicating limited predictive agreement under the tested hybrid configuration.

Pearson R in Figure 5 describes the strength of the linear association between derived and predicted CCC for the hybrid PROSAIL–GPR models and should not be interpreted as equivalent to the predictive R^2 reported in Table 6. For example, at Site B in July, the hybrid model showed a relatively strong Pearson correlation ($R = 0.65$), despite substantially poorer cross-validated predictive performance according to R^2, RMSE, and NRMSE (Table 6). The corresponding empirical GPR model had a slightly lower Pearson correlation ($R = 0.60$;

Figure 3) but substantially better predictive performance (Table 5). This illustrates that a comparatively strong linear association does not necessarily indicate close predictive agreement. Accordingly, the empirical and hybrid approaches are compared primarily using the tree-grouped cross-validated R^2, RMSE, and NRMSE, with Pearson R used as a complementary measure of association.

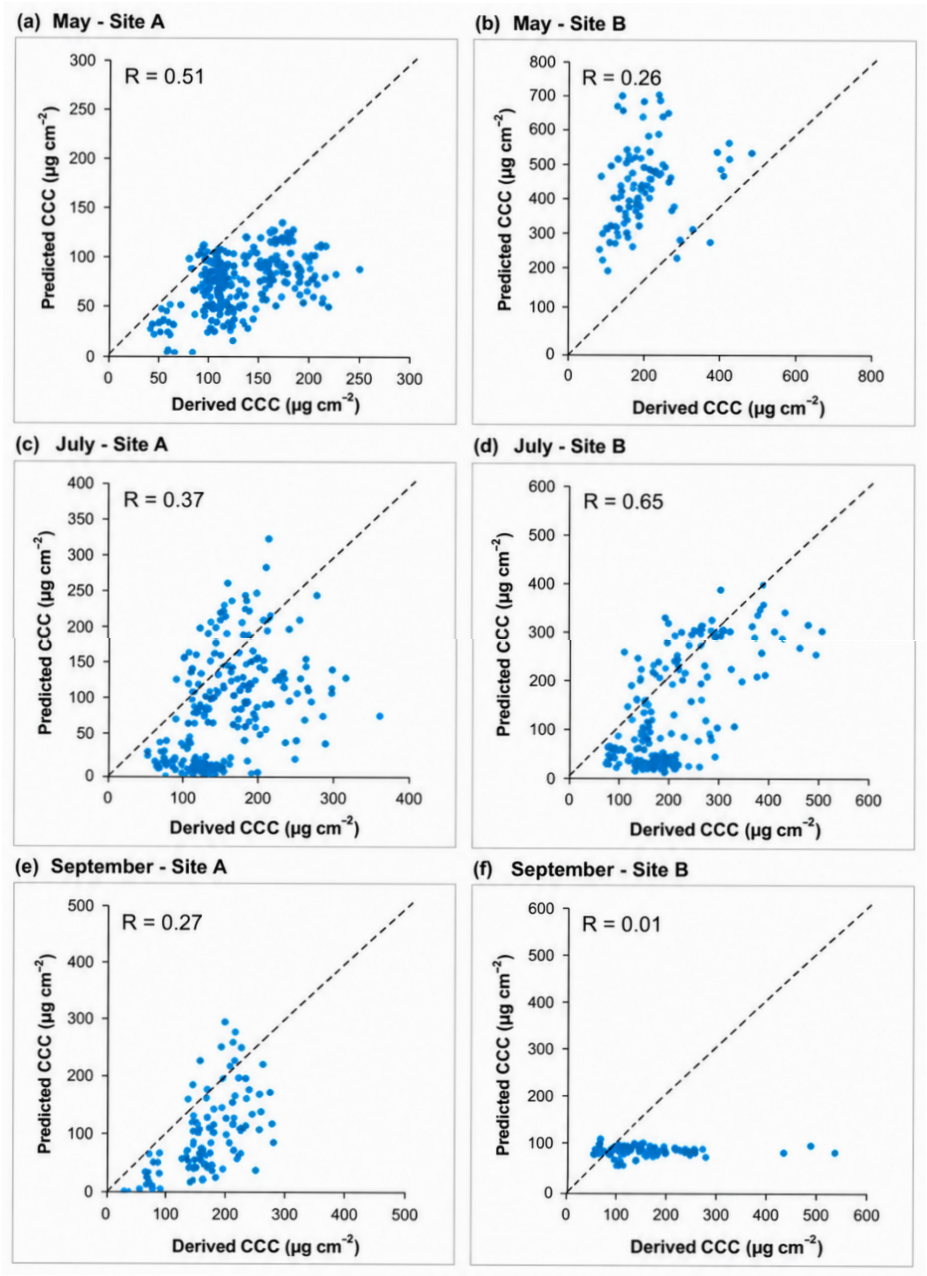


Figure 5. Relationships between derived and predicted canopy chlorophyll content per unit ground area (CCC) for the hybrid PROSAIL–GPR models under tree-grouped three-fold cross-validation across sites and sampling periods. Pearson R describes the linear association between derived and predicted CCC; predictive R^2, RMSE, and NRMSE are reported in Table 6. The dashed line represents the 1:1 relationship and is provided as a visual reference for agreement rather than as a fitted regression.

Overall, these results demonstrate lower predictive performance of the tested PROSAIL–GPR implementation relative to the corresponding empirical GPR models under the four-band UAV configuration examined here when evaluated using the primary tree-grouped predictive metrics (R^2, RMSE, and NRMSE). The results do not, however, establish a single

causal explanation for this difference. Potential contributions from PROSAIL parameterization and model assumptions, limited spectral information, canopy structural complexity, the number of independent training trees, acquisition conditions, uncertainty in the derived CCC response variable, and the integration of simulated and observational information are therefore considered as alternative and potentially interacting explanations in Section 4.

Spatial predictions from the hybrid PROSAIL–GPR model showed substantial within-stand variation in retrieved CCC (Figure 6). Compared with the empirical GPR maps, the hybrid predictions exhibited different spatial distributions and ranges of CCC. These differences are interpreted as characteristics of the respective retrieval approaches rather than as evidence of differences in OLB infestation or forest-health condition. Because OLB abundance and damage severity were not quantitatively measured, the hybrid maps represent spatial variation in retrieved CCC rather than direct estimates of pest infestation or damage severity.

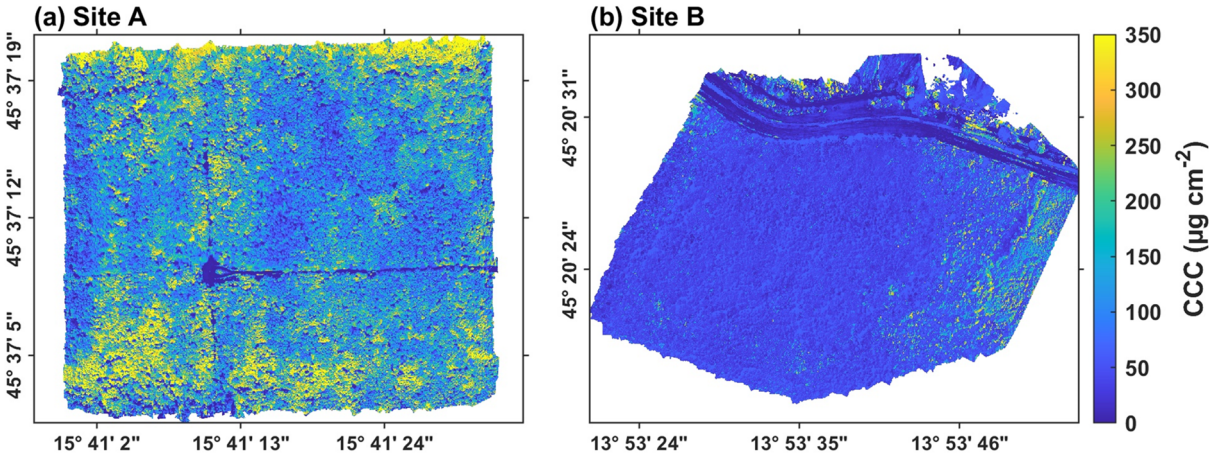


Figure 6. Spatial distribution of canopy chlorophyll content per unit ground area (CCC; µg cm^{-2}) predicted using the hybrid PROSAIL–GPR model for July 2022 at (**a**) Site A and (**b**) Site B. The maps represent spatial variation in retrieved CCC and should not be interpreted as direct estimates of OLB infestation or damage severity.

4. Discussion

4.1. Empirical CCC Retrieval and Seasonal Variation

The principal contribution of this study lies in the direct comparison of empirical and physically constrained CCC retrieval using the same four-band, very-high-spatial-resolution UAV observations of structurally heterogeneous oak canopies. Although empirical machine learning, PROSAIL, GPR, and hybrid RTM–ML retrieval are established approaches, their comparative performance under crown-scale observations with limited spectral information remains an important question. Under these conditions, the tested PROSAIL–GPR implementation did not provide a retrieval advantage over the empirical approaches. This finding is specific to the investigated sensor, canopy conditions, model configuration, and validation framework and does not establish the general superiority of empirical methods.

Tree-grouped cross-validation resulted in more moderate empirical retrieval performance than observation-level validation and revealed greater variation among algorithms, sites, and sampling periods. By retaining all crown-aspect and repeated observations from each tree within a single fold, this approach provided a more stringent assessment of generalization to held-out trees and reduced the risk of overly optimistic performance estimates caused by tree-level dependence.

No single empirical algorithm was consistently optimal across all site × month combinations. GPR performed particularly well at Site A in May and July, whereas RF performed

best under several other conditions, including Site A in September, and achieved the highest R^2 at Site B in July. LSLR produced the lowest prediction error at Site B in July, while KRR achieved the highest R^2 at Site B in September. These differences indicate that no single regression structure consistently represented the relationship between four-band reflectance and derived CCC across sites and sampling periods.

The performance of GPR is consistent with its capacity to represent nonlinear relationships without a predefined functional form, which may be advantageous when reflectance is influenced by biochemical properties, canopy structure, illumination, and background contributions, particularly with limited training samples [5,8]. RF provides complementary advantages by accommodating nonlinear interactions and heterogeneous predictor–response relationships with relatively few distributional assumptions. Together, these results support the usefulness of flexible nonlinear methods without identifying a universally optimal algorithm.

Seasonal differences in retrieval performance indicate that the spectral–CCC relationship varied among sampling periods. However, because the sites differed in geographic location, stand characteristics, environmental conditions, and infestation status, and acquisition geometry varied among campaigns, these differences cannot be attributed exclusively to OLB effects or phenology. The spatial predictions nevertheless demonstrated substantial within-stand variation in derived CCC, with lower predicted values in portions of the visibly damaged canopy at Site A and generally higher values at Site B. These patterns represent variation in a derived canopy chlorophyll metric, not direct estimates of OLB infestation or damage severity, which were not quantitatively measured.

4.2. Performance of the Hybrid PROSAIL–GPR Approach

The hybrid PROSAIL–GPR approach generally produced higher prediction errors and lower predictive performance than the empirical approaches under tree-grouped validation. Although hybrid RTM–ML approaches combine statistical learning with physically plausible relationships from radiative-transfer simulations [11,31,32], this expected advantage was not consistently realized with the four-band UAV observations.

Predictive agreement must also be distinguished from linear association. At Site B in July, the hybrid PROSAIL–GPR model produced a Pearson R of 0.65, slightly higher than the corresponding empirical GPR value of 0.60, despite substantially poorer predictive performance according to cross-validated R^2, RMSE, and NRMSE. Thus, correlation alone does not establish predictive accuracy, and the tree-grouped cross-validated metrics provide the primary basis for comparing approaches.

Sensitivity tests showed that expanding the Cab and LAI parameter domains or constraining them using training-tree information did not systematically improve hybrid retrieval (Table 6). Training-tree-informed parameterization improved performance for some site × month combinations but produced little improvement or poorer performance for others. Incomplete parameter-space coverage may therefore have contributed to individual errors but does not adequately explain the overall empirical–hybrid performance difference.

Active learning retained different numbers of simulations across cross-validation folds, indicating sensitivity of the optimized LUT to the available training trees. Because AL and LUT optimization were repeated independently within each training fold, this variation also highlights the influence of the limited number of independent trees, despite the larger number of crown-aspect observations.

The poorer performance of the hybrid approach cannot be attributed to a single mechanism. Potential contributors include PROSAIL parameterization, the limited four-band spectral configuration, the number and variability of independent training trees, the active-learning and LUT-selection procedure, uncertainty in the derived CCC response variable,

acquisition geometry, and differences between the canopy representation assumed by PROSAIL and the structure observed by the UAV. Because no ablation analysis was performed, their relative contributions cannot be quantified. Accordingly, the findings demonstrate a limitation of the tested PROSAIL–GPR configuration under the investigated conditions, not an inherent limitation of hybrid RTM–ML retrieval in forests.

4.3. Effects of Canopy Structure, Spectral Dimensionality, and Acquisition Conditions

One plausible contributor to hybrid-model performance is the representation of canopy structure. PROSAIL couples leaf optical properties represented by PROSPECT with the 4SAIL canopy model, which assumes a horizontally homogeneous turbid medium. In contrast, mature oak crowns contain foliage clumping, gaps, branches, woody components, overlapping crown elements, and spatially variable illuminated and shaded foliage, potentially altering canopy reflectance relative to homogeneous model assumptions [14–17,19].

Very-high-resolution crown-aspect observations resolve structural features and shadows that are averaged within coarser pixels, potentially increasing mismatch between simulated and observed reflectance. However, without a direct comparison against a suitably parameterized three-dimensional RTM, structural mismatch cannot be identified as the primary cause of lower hybrid performance [14,15,19].

The limited spectral dimensionality of the Parrot Sequoia may have further constrained the hybrid retrieval. Although PROSAIL generates spectrally continuous simulations, these were resampled to the same four UAV bands used by the empirical models, ensuring equivalent spectral information but limiting the ability to distinguish biochemical, structural, background, and illumination effects that produce similar reflectance. Hyperspectral observations could provide additional constraints, although they would not independently resolve structural mismatch.

Empirical models instead learned relationships directly between four-band reflectance and derived CCC without imposing a prescribed canopy representation. This flexibility may have contributed to their performance, although the partial dependence of derived CCC on UAV spectral information must also be considered (Section 4.4).

Differences in solar illumination geometry among acquisition dates represent an additional source of uncertainty. Variation in solar zenith angle may have changed illuminated and shaded crown proportions and canopy reflectance through bidirectional reflectance effects, particularly at very high spatial resolution [14,15]. Site- and month-specific modeling reduced the mixing of observations acquired under different conditions but did not eliminate BRDF-related effects or separate illumination from phenological influences.

4.4. Uncertainty Associated with the Derived CCC Response Variable

An important consideration in interpreting the retrieval results is that CCC was a derived response variable rather than an independently measured canopy-level reference. LCC was derived from field SPAD measurements using the species-specific calibration for pedunculate oak, whereas LAI was estimated from UAV-derived NDRE and the photogrammetrically derived CHM. CCC was subsequently calculated as LCC × LAI. Thus, CCC represents chlorophyll content per unit ground area ($\mu g\ cm^{-2}$ ground area), distinct from LCC expressed per unit leaf area ($\mu g\ cm^{-2}$ leaf area), and should be interpreted as a derived canopy-level chlorophyll metric.

The LAI estimates were not independently validated against field LAI measurements at the study sites. Potential uncertainties include reduced NDRE sensitivity at high canopy density and errors in photogrammetric terrain reconstruction beneath dense foliage, which propagate through the DTM, CHM, LAI, and ultimately derived CCC [57].

The Site B LAI pattern illustrates why these estimates should be interpreted cautiously. Mean UAV-estimated LAI was slightly higher in May than in July, but the monthly datasets differed in campaign composition and therefore cannot establish a within-year phenological trend. This pattern persisted after tree-level aggregation, excluding the treatment of crown aspects as independent observations as its explanation; nevertheless, LAI accuracy remains uncertain without field validation.

Additional uncertainty arises from transferring the empirical LAI equation of [50] to pedunculate oak forests. Their relationship was calibrated using 30 field LAI observations in South Korean forest and landscaped tree stands, including pine- and chestnut-dominated vegetation, and achieved $R^2 = 0.496$ using NDRE and CHM. Although the study employed a comparable four-band UAV sensor and photogrammetric canopy-height information, it did not establish a transferable LAI applicability range or independently validate the equation for pedunculate oak. Differences in species composition, canopy architecture, and environmental conditions may therefore affect its applicability and propagate uncertainty into derived CCC.

Both retrieval approaches were evaluated against the same derived CCC response, but LAI uncertainty may affect them differently. In the empirical models, LAI contributed directly to CCC calculation, whereas in the training-tree-informed hybrid configuration, the same derived LAI values also informed the PROSAIL parameter range used to generate simulated reflectance and CCC combinations for LUT optimization and active-learning selection. Consequently, the common response variable supports a consistent comparison but does not eliminate potentially different effects of LAI uncertainty.

A further limitation is the partial dependence between the empirical predictors and derived CCC. NDRE, calculated from two UAV bands, contributed to the LAI estimate, while those bands were also used as empirical reflectance predictors. Although NDRE itself was not an empirical predictor, this shared spectral information may have contributed to empirical retrieval performance. Therefore, the empirical–hybrid difference cannot be interpreted solely as a difference in intrinsic model capability.

Independent LAI measurements from field observations, terrestrial or UAV LiDAR, hemispherical photography, or other canopy-structure methods would improve validation and support a CCC reference less dependent on the UAV spectral predictors.

4.5. Implications for UAV-Based CCC Retrieval and Future Directions

The results demonstrate that spatial variation in derived CCC can be retrieved from very-high-resolution four-band UAV imagery in structurally heterogeneous oak stands, although retrieval performance varied with site, sampling period, and modeling approach. Empirical methods offer a relatively direct retrieval strategy when representative calibration observations are available, whereas the tested PROSAIL–GPR configuration provided no overall advantage according to tree-grouped cross-validated R^2, RMSE, and NRMSE.

Tree-grouped validation supports generalization to held-out trees within the sampled stands and campaigns, but not necessarily to independent forest stands, geographic regions, or canopy types.

The present results also distinguish demonstrated CCC retrieval capability from its potential application to forest-health monitoring. Sites A and B differed in location, stand and environmental conditions, and OLB pressure, while quantitative measurements of pest abundance, damage severity, and defoliation were unavailable. Accordingly, CCC differences cannot be causally attributed to OLB, and the maps should not be interpreted as direct measures of infestation, damage severity, or forest-health status. Their potential value for OLB-related stress monitoring requires independent validation.

The four UAV bands were modeled jointly, and their spectral correlation and nonlinear interactions prevent attribution of GPR performance to individual bands from the present analysis. Permutation importance or leave-one-band-out evaluation would be needed to quantify band-specific contributions, beyond the scope of this empirical–hybrid comparison.

Future research should combine larger and more diverse tree samples with independent LAI and canopy-structure measurements, quantitative OLB abundance and damage assessments, and validation across additional stands and infestation levels. Hyperspectral observations could test whether greater spectral information improves hybrid retrieval, while three-dimensional RTMs could evaluate the effects of crown geometry, foliage clumping, woody components, and shadowing. Explicit consideration of illumination geometry and BRDF effects would also help distinguish acquisition-related variation from phenological responses.

Overall, the findings emphasize that retrieval performance depends on compatibility among canopy structure, spectral and spatial resolution, model assumptions, reference-variable characteristics, sample independence, and acquisition conditions rather than model complexity alone.

5. Conclusions

This study compared empirical machine-learning and hybrid PROSAIL–GPR approaches for retrieving derived canopy chlorophyll content per unit ground area (CCC) from four-band, very-high-spatial-resolution UAV imagery of structurally heterogeneous pedunculate oak canopies. Under tree-grouped cross-validation, empirical retrieval performance varied among algorithms, sites, and sampling periods, with no single algorithm consistently performing best. GPR, RF, LSLR, and KRR achieved the strongest results under different conditions and metrics, while spatial predictions revealed substantial within-stand variation in derived CCC.

The principal contribution of this study is the direct comparison of empirical and physically constrained retrieval using the same limited-band, crown-scale observations and tree-grouped validation framework. According to the primary cross-validated predictive metrics (R^2, RMSE, and NRMSE), the tested PROSAIL–GPR implementation did not improve overall predictive performance relative to the empirical approaches. This result may reflect interacting effects of limited spectral information, canopy complexity, PROSAIL representation and parameterization, independent training-tree availability, acquisition geometry, active-learning and LUT configuration, and uncertainty in derived CCC. Their individual contributions were not isolated, and the findings do not establish a general limitation of hybrid RTM–ML retrieval.

CCC was derived from field-based LCC and UAV-estimated LAI rather than independently measured, introducing uncertainty associated with LAI estimation, equation transferability, and partial dependence on the empirical spectral predictors. The retrieved CCC patterns should be interpreted as spatial variation in a derived canopy-level chlorophyll metric rather than as direct estimates of OLB infestation, damage severity, or forest-health condition. Independent LAI validation and quantitative pest measurements are needed before CCC can be established as an indicator of OLB-related stress.

Overall, the findings emphasize model–observation compatibility rather than model complexity alone when selecting retrieval strategies for very-high-resolution forest imagery. Future evaluation using independent canopy measurements, more diverse tree samples, richer spectral information, and three-dimensional radiative-transfer representations will help establish when physically constrained retrieval provides additional value in complex forest canopies.

Author Contributions: Conceptualization, N.Z., A.S.M. and I.B.; methodology, N.Z., A.S.M. and J.V.; software, N.Z. and J.V.; validation, N.Z., A.S.M. and I.B.; formal analysis, N.Z.; investigation, N.Z. and D.M.; resources, A.S.M., D.M. and A.S.; data curation, N.Z.; writing—original draft preparation, N.Z.; writing—review and editing, A.S.M., J.V., D.M., A.S. and I.B.; visualization, N.Z.; supervision, A.S.M., D.M. and I.B.; project administration, I.B.; funding acquisition, I.B. and D.M. All authors have read and agreed to the published version of the manuscript.

Funding: This research was funded by the European Union–NextGenerationEU under the Recovery and Resilience Plan for Croatia (Ministry of Science, Education and Youth), within the project No. 400-01/23-01/6-1 "Establishment and development of the Laboratory for Remote Research and Geoinformation in Forestry and Environment (LabDIG)".

Data Availability Statement: The minimum dataset supporting the findings and conclusions of this study is openly available in Zenodo at https://doi.org/10.5281/zenodo.22670866. The UAV orthomosaics and radiative transfer model outputs are available from the corresponding author upon reasonable request because of their large file size and associated data-processing requirements.

Acknowledgments: The authors would like to thank Bowling Green State University in Ohio for providing a multispectral drone for this study, and the funding agencies that supported this work, including Croatian Ministry of Agriculture, Forestry and Fishery.

Conflicts of Interest: The authors declare no conflicts of interest.

References

1. Hall, R.J.; Castilla, G.; White, J.C.; Cooke, B.J.; Skakun, R.S. Remote sensing of forest pest damage: A review and lessons learned from a Canadian perspective. *Can. Entomol.* **2016**, *148*, S296–S356. [CrossRef]
2. Pontius, J.; Hallett, R. Comprehensive Methods for Earlier Detection and Monitoring of Forest Decline. *For. Sci.* **2014**, *60*, 1156–1163. [CrossRef]
3. Duarte, A.; Borralho, N.; Cabral, P.; Caetano, M. Recent advances in forest insect pests and diseases monitoring using UAV-based data: A systematic review. *Forests* **2022**, *13*, 911. [CrossRef]
4. Ecke, S.; Dempewolf, J.; Frey, J.; Schwaller, A.; Endres, E.; Klemmt, H.J.; Tiede, D.; Seifert, T. UAV-based forest health monitoring: A systematic review. *Remote Sens.* **2022**, *14*, 3205. [CrossRef]
5. Verrelst, J.; Muñoz, J.; Alonso, L.; Delegido, J.; Rivera, J.P.; Camps-Valls, G.; Moreno, J. Machine learning regression algorithms for biophysical parameter retrieval: Opportunities for Sentinel-2 and -3. *Remote Sens. Environ.* **2012**, *118*, 127–139. [CrossRef]
6. Zhang, Y.; Ma, J.; Liang, S.; Li, X.; Li, M. An Evaluation of Eight Machine Learning Regression Algorithms for Forest Aboveground Biomass Estimation from Multiple Satellite Data Products. *Remote Sens.* **2020**, *12*, 4015. [CrossRef]
7. Angel, Y.; McCabe, M.F. Machine Learning Strategies for the Retrieval of Leaf-Chlorophyll Dynamics: Model Choice, Sequential Versus Retraining Learning, and Hyperspectral Predictors. *Front. Plant Sci.* **2022**, *13*, 722442. [CrossRef] [PubMed]
8. Alam, M.M.T.; Simic Milas, A.; Gašparović, M.; Osei, H.P. Retrieval of Crop Canopy Chlorophyll: Machine Learning vs. Radiative Transfer Model. *Remote Sens.* **2024**, *16*, 2058. [CrossRef]
9. Cardil, A.; Otsu, K.; Pla, M.; Silva, C.A.; Brotons, L. Quantifying pine processionary moth defoliation in a pine-oak mixed forest using unmanned aerial systems and multispectral imagery. *PLoS ONE* **2019**, *14*, e0213027. [CrossRef] [PubMed]
10. Yu, R.; Luo, Y.; Zhou, Q.; Zhang, X.; Wu, D.; Ren, L. Early detection of pine wilt disease using deep learning algorithms and UAV-based multispectral imagery. *For. Ecol. Manag.* **2021**, *497*, 119493. [CrossRef]
11. Verrelst, J.; Malenovský, Z.; Van der Tol, C.; Camps-Valls, G.; Gastellu-Etchegorry, J.-P.; Lewis, P.; North, P.; Moreno, J. Quantifying vegetation biophysical variables from imaging spectroscopy data: A review on retrieval methods. *Surv. Geophys.* **2019**, *40*, 589–629. [CrossRef] [PubMed]
12. Kattenborn, T.; Schmidtlein, S. Radiative transfer modelling reveals why canopy reflectance follows function. *Sci. Rep.* **2019**, *9*, 6541. [CrossRef] [PubMed]
13. Jacquemoud, S.; Verhoef, W.; Baret, F.; Bacour, C.; Zarco-Tejada, P.J.; Asner, G.P.; François, C.; Ustin, S.L. PROSPECT+SAIL models: A review of use for vegetation characterization. *Remote Sens. Environ.* **2009**, *113*, S56–S66. [CrossRef]
14. Li, X.; Strahler, A.H. Geometric-optical bidirectional reflectance modeling of the discrete crown vegetation canopy: Effect of crown shape and mutual shadowing. *IEEE Trans. Geosci. Remote Sens.* **1992**, *30*, 276–292. [CrossRef]
15. Huemmrich, K.F. The GeoSail model: A simple addition to the SAIL model to describe discontinuous canopy reflectance. *Remote Sens. Environ.* **2001**, *75*, 423–431. [CrossRef]
16. Rautiainen, M.; Stenberg, P. Application of photon recollision probability in coniferous canopy reflectance simulations. *Remote Sens. Environ.* **2005**, *96*, 98–107. [CrossRef]

17. Mõttus, M.; Stenberg, P.; Rautiainen, M. Photon recollision probability in heterogeneous forest canopies: Compatibility with a hybrid GO model. *J. Geophys. Res. Atmos.* **2007**, *112*, D03104. [CrossRef]
18. Zarco-Tejada, P.J.; Hornero, A.; Beck, P.S.A.; Kattenborn, T.; Kempeneers, P.; Hernández-Clemente, R. Chlorophyll content estimation in an open-canopy conifer forest with Sentinel-2A and hyperspectral imagery in the context of forest decline. *Remote Sens. Environ.* **2019**, *223*, 320–335. [CrossRef] [PubMed]
19. Wu, Q.; Yang, S.; Jiang, J. Impacts of clumping effect on canopy reflectance using 3D radiative transfer modeling. *Front. For. Glob. Change* **2023**, *6*, 1106773. [CrossRef]
20. Schlerf, M.; Atzberger, C. Inversion of a forest reflectance model to estimate structural canopy variables from hyperspectral remote sensing data. *Remote Sens. Environ.* **2006**, *100*, 281–294. [CrossRef]
21. Sibiya, B.S.; Odindi, J.; Mutanga, O.; Cho, M.A.; Masemola, C.R. The utility of radiative transfer models (RTM) on remotely sensed data in retrieving biophysical and biochemical properties of terrestrial biomes: A systematic review. *Adv. Space Res.* **2025**, *75*, 7424–7444. [CrossRef]
22. Widlowski, J.-L.; Pinty, B.; Lopatka, M.; Atzberger, C.; Buzica, D.; Chelle, M.; Disney, M.; Gastellu-Etchegorry, J.-P.; Gerboles, M.; Gobron, N.; et al. The fourth radiation transfer model intercomparison (RAMI-IV): Proficiency testing of canopy reflectance models with ISO-13528. *J. Geophys. Res. Atmos.* **2013**, *118*, 6869–6890. [CrossRef]
23. Ali, A.M.; Skidmore, A.K.; Darvishzadeh, R.; van Duren, I.; Holzwarth, S.; Mueller, J. Retrieval of forest leaf functional traits from HySpex imagery using radiative transfer models and continuous wavelet analysis. *ISPRS J. Photogramm. Remote Sens.* **2016**, *122*, 68–80. [CrossRef]
24. Ebengo, D.M.; de Boissieu, F.; Vincent, G.; Weber, C.; Féret, J.-B. Simulating imaging spectroscopy in tropical forest with 3D radiative transfer modeling. *Remote Sens.* **2021**, *13*, 2120. [CrossRef]
25. Wang, Z.; Skidmore, A.K.; Darvishzadeh, R.; Wang, T. Mapping forest canopy nitrogen content by inversion of coupled leaf-canopy radiative transfer models from airborne hyperspectral imagery. *Agric. For. Meteorol.* **2018**, *253–254*, 247–260. [CrossRef]
26. Miraglio, T.; Coops, N.C.; Blanchet, F.G.; Kalacska, M.; Arroyo-Mora, J.P.; Laliberté, E.; Vaglio Laurin, G. Mapping canopy traits over Québec using airborne and spaceborne imaging spectroscopy. *Sci. Rep.* **2023**, *13*, 17179. [CrossRef] [PubMed]
27. Darvishzadeh, R.; Skidmore, A.K.; Abdullah, H.; Weldemariam, E.C.; Ali, A.M.; Wang, T.; Nieuwenhuis, W.; Heurich, M.; Vrieling, A.; O'Connor, B.; et al. Mapping leaf chlorophyll content from Sentinel-2 and RapidEye data in spruce stands using the invertible forest reflectance model. *Int. J. Appl. Earth Obs. Geoinf.* **2019**, *79*, 58–70. [CrossRef]
28. Lin, Q.; Huang, H.; Wang, J.; Huang, K.; Liu, Y. Detection of pine shoot beetle (PSB) stress on pine forests at individual tree level using UAV-based hyperspectral imagery and lidar. *Remote Sens.* **2019**, *11*, 2540. [CrossRef]
29. Li, X.; Tong, T.; Luo, T.; Wang, J.; Rao, Y.; Li, L.; Jin, D.; Wu, D.; Huang, H. Retrieving the infected area of pine wilt disease-disturbed pine forests from medium-resolution satellite images using the stochastic radiative transfer theory. *Remote Sens.* **2022**, *14*, 1526. [CrossRef]
30. Caicedo, J.P.R.; Verrelst, J.; Muñoz-Marí, J.; Moreno, J.; Camps-Valls, G. Toward a Semiautomatic Machine Learning Retrieval of Biophysical Parameters. *IEEE J. Sel. Top. Appl. Earth Obs. Remote Sens.* **2014**, *7*, 1249–1259. [CrossRef]
31. Verrelst, J.; Dethier, S.; Rivera, J.P.; Muñoz-Marí, J.; Camps-Valls, G.; Moreno, J. Active learning methods for efficient hybrid biophysical variable retrieval. *IEEE Geosci. Remote Sens. Lett.* **2016**, *13*, 1012–1016. [CrossRef]
32. Berger, K.; Verrelst, J.; Féret, J.-B.; Hank, T.; Wocher, M.; Mauser, W.; Camps-Valls, G. Retrieval of aboveground crop nitrogen content with a hybrid machine learning method. *Int. J. Appl. Earth Obs. Geoinf.* **2020**, *92*, 102174. [CrossRef] [PubMed]
33. Tagliabue, G.; Boschetti, M.; Bramati, G.; Candiani, G.; Colombo, R.; Nutini, F.; Pompilio, L.; Rivera-Caicedo, J.P.; Rossi, M.; Rossini, M.; et al. Hybrid retrieval of crop traits from multi-temporal PRISMA hyperspectral imagery. *ISPRS J. Photogramm. Remote Sens.* **2022**, *187*, 362–377. [CrossRef]
34. Sun, J.; Shi, S.; Wang, L.; Li, H.; Wang, S.; Gong, W.; Tagesson, T. Optimizing LUT-based inversion of leaf chlorophyll from hyperspectral lidar data: Role of cost functions and regulation strategies. *Int. J. Appl. Earth Obs. Geoinf.* **2021**, *105*, 102602. [CrossRef]
35. Tsele, P.; Ramoelo, A. Hybrid retrieval of grass biophysical variables based-on radiative transfer, active learning and regression methods using Sentinel-2 data in Marakele National Park. *Geocarto Int.* **2024**, *39*, 2387087. [CrossRef]
36. Debue, M.; Vincent, G.; Alleaume, S.; de Boissieu, F.; Briottet, X.; Féret, J.-B.; Gastellu-Etchegorry, J.-P.; Limousin, J.-M.; Longepierre, D.; Adeline, K. Adequacy of Mediterranean forest simulations from DART radiative transfer model and UAV laser scanning data to hyperspectral images. In *Remote Sensing for Agriculture, Ecosystems, and Hydrology*; SPIE: Bellingham, WA, USA, 2023. [CrossRef]
37. Zhou, Y.; Li, X.; Chen, C.; Zhou, L.; Zhao, Y.; Chen, J.; Tan, C.; Sun, J.; Zhang, L.; Hu, M.; et al. Coupling the PROSAIL model and machine learning approach for canopy parameter estimation of Moso bamboo forests from UAV hyperspectral data. *Forests* **2024**, *15*, 946. [CrossRef]
38. Shen, X.; Cao, L.; Coops, N.C.; Fan, H.; Wu, X.; Liu, H.; Wang, G.; Cao, F. Quantifying vertical profiles of biochemical traits for forest plantation species using advanced remote sensing approaches. *Remote Sens. Environ.* **2020**, *250*, 112041. [CrossRef]

39. Zhang, C.; Chen, Z.; Yang, G.; Xu, B.; Feng, H.; Chen, R.; Qi, N.; Zhang, W.; Zhao, D.; Cheng, J.; et al. Removal of canopy shadows improved retrieval accuracy of individual apple tree crowns LAI and chlorophyll content using UAV multispectral imagery and PROSAIL model. *Comput. Electron. Agric.* **2024**, *221*, 108959. [CrossRef]
40. Xu, L.; Shi, S.; Gong, W.; Shi, Z.; Qu, F.; Tang, X.; Chen, B.; Sun, J. Improving leaf chlorophyll content estimation through constrained PROSAIL model from airborne hyperspectral and LiDAR data. *Int. J. Appl. Earth Obs. Geoinf.* **2022**, *115*, 103128. [CrossRef]
41. Zhao, X.; Qi, J.; Jiang, J.; Liu, S.; Xu, H.; Lin, S.; Yu, Z.; Li, L.; Huang, H. Fine-scale retrieval of leaf chlorophyll content using a semi-empirically accelerated 3D radiative transfer model. *Int. J. Appl. Earth Obs. Geoinf.* **2024**, *135*, 104285. [CrossRef]
42. Zhang, C.; Li, P.; Zhang, S.; Wang, P. Three-dimensional chlorophyll content retrieval in forest canopies via physics guided transfer learning and UAV multi-source remote sensing. *Sci. Remote Sens.* **2026**, *13*, 100443. [CrossRef]
43. Paulin, M.; Hirka, A.; Eötvös, C.B.; Gáspár, C.; Fürjes-Mikó, Á.; Csóka, G. Known and predicted impacts of the invasive oak lace bug (*Corythucha arcuata*) in European oak ecosystems—A review. *Folia Oecol.* **2020**, *47*, 131–139. [CrossRef]
44. Csóka, G.; Hirka, A.; Mutun, S.; Glavendekić, M.; Mikó, Á.; Szőcs, L.; Paulin, M.; Eötvös, C.B.; Gáspár, C.; Csepelényi, M.; et al. Spread and potential host range of the invasive oak lace bug [*Corythucha arcuata* (Say, 1832)—Heteroptera: Tingidae] in Eurasia. *Agric. For. Entomol.* **2020**, *22*, 61–74. [CrossRef]
45. Ciceu, A.; Bălăcenoiu, F.; de Groot, M.; Chakraborty, D.; Avtzis, D.; Barta, M.; Blaser, S.; Bracalini, M.; Castagneyrol, B.; Chernova, U.A.; et al. The ongoing range expansion of the invasive oak lace bug across Europe: Current occurrence and potential distribution under climate change. *Sci. Total Environ.* **2024**, *949*, 174950. [CrossRef] [PubMed]
46. Nikolić, N.; Pilipović, A.; Drekić, M.; Kojić, D.; Poljaković-Pajnik, L.; Orlović, S.; Arsenov, D. Physiological responses of Pedunculate oak (*Quercus robur* L.) to *Corythucha arcuata* (Say, 1832) attack. *Arch. Biol. Sci.* **2019**, *71*, 167–176. [CrossRef]
47. Bălăcenoiu, F.; Toma, D.; Nețoiu, C. From Field Data to Practical Knowledge: Investigating the Bioecology of the Oak Lace Bug—An Invasive Insect Species in Europe. *Insects* **2023**, *14*, 882. [CrossRef] [PubMed]
48. Zorić, N.; Franjević, M.; Matošević, D. Further spread of *Corythucha arcuata* (Hemiptera; Tingidae) in Croatia. *South-East Eur. For.* **2023**, *14*, 111–115. [CrossRef]
49. Brown, L.A.; Williams, O.; Dash, J. Calibration and characterisation of four chlorophyll meters and transmittance spectroscopy for non-destructive estimation of forest leaf chlorophyll concentration. *Agric. For. Meteorol.* **2022**, *323*, 109059. [CrossRef]
50. Moon, H.-G.; Choi, T.-Y.; Kang, D.-I.; Cha, J.-G. Study on the Estimation of leaf area index (LAI) of using UAV vegetation index and Tree Height data. *J. Korean Assoc. Geogr. Inf. Stud.* **2018**, *21*, 158–174. [CrossRef]
51. Watson, G.S. Linear Least Squares Regression. *Ann. Math. Stat.* **1967**, *38*, 1679–1699. [CrossRef]
52. Suykens, J.; Vandewalle, J. Least Squares Support Vector Machine Classifiers. *Neural Process. Lett.* **1999**, *9*, 293–300. [CrossRef]
53. Loh, W.-Y. Classification and regression trees. *WIREs Data Min. Knowl. Discov.* **2011**, *1*, 14–23. [CrossRef]
54. Breiman, L. Random Forests. *Mach. Learn.* **2001**, *45*, 5–32. [CrossRef]
55. Haykin, S. *Neural Networks: A Comprehensive Foundation*, 1st ed.; Prentice Hall PTR: Hoboken, NJ, USA, 1994.
56. Rasmussen, C.E.; Williams, C.K.I. *Gaussian Processes for Machine Learning*; MIT Press: Cambridge, MA, USA, 2008.
57. Wallace, L.; Lucieer, A.; Malenovský, Z.; Turner, D.; Vopěnka, P. Assessment of forest structure using two UAV techniques: A comparison of airborne laser scanning and structure from motion point clouds. *Forests* **2016**, *7*, 62. [CrossRef]

Disclaimer/Publisher's Note: The statements, opinions and data contained in all publications are solely those of the individual author(s) and contributor(s) and not of MDPI and/or the editor(s). MDPI and/or the editor(s) disclaim responsibility for any injury to people or property resulting from any ideas, methods, instructions or products referred to in the content.